ijrr

The International Journal of
Robotics Research
31(8) 974–996

DOI: 10.1177/0278364912442096
ijr.sagepub.com
SAGE

A bioinspired dynamical vertical climbing robot

Goran A Lynch[1], Jonathan E Clark[2], Pei-Chun Lin[3] and Daniel E Koditschek[1]

Abstract

This paper describes the inspiration for, design, analysis, and implementation of, and experimentation with the first dynamical vertical climbing robot. Biologists have proposed a pendulous climbing model that abstracts remarkable similarities in dynamical wall scaling behavior exhibited by radically different animal species. We numerically study a version of that pendulous climbing template dynamically scaled for applicability to utilitarian payloads with conventional electronics and actuation. This simulation study reveals that the incorporation of passive compliance can compensate for the scaled model's poorer power density and scale disadvantages relative to biology. However, the introduction of additional dynamical elements raises new concerns about stability regarding both the power stroke and limb coordination schemes that we allay via mathematical analysis of further simplified models. Combining these numerical and analytical insights into a series of design prototypes, we document the correspondence of the various models to the scaled platforms and report that our final prototype climbs dynamically at vertical speeds up to 0.67 m/s (1.5 body-lengths per second, in rough agreement with our models' predictions).

Keywords

Dynamic climbing, legged locomotion, robot design

1. Introduction

Past climbing robots have been slow and in most instances restricted to surfaces where specific attachment mechanisms such as suction and electromagnetic adhesion can be brought to bear (Balaguer et al. 2000; La Rosa et al. 2002). Over the last decade robots have been built that are capable of more broadly effective attachment, for example by means of actively grasped footholds (Bevly et al. 2000; Bretl et al. 2003), or passively exploited asperities Autumn et al. (2005), or vectored thrust (Xiao et al. 2005). The last few years have also seen the revival of rimless wheels with sticky toes (Daltorio et al. 2005; Murphy and Sitti 2007; Murphy et al. 2011) to intermittently 'roll' up smooth walls[1] (Bekey 2005) and the development of novel spined and sticky feet for attachment to smooth surfaces such as concrete and brick (Asbeck et al. 2006; Spenko et al. 2008). Despite the dramatic improvement of attachment technologies, robotic climbers still generally progress slowly up vertical surfaces.

The unremitting cost of work against gravity seems significantly less constraining in the animal kingdom, which boasts a variety of species that can rapidly maneuver their way up vertical environments surfaced in a broad variety of materials, textures, and geometries. Recent biomechanical studies of small, agile climbing animals reveal a striking similarity in locomotion dynamics that belies stark differences in attachment mechanisms, morphology, and phylogeny (Goldman et al. 2006). These unexpectedly common patterns can be abstracted in a simple numerical model that raises the prospect of a 'template' (Full and Koditschek 1999) for dynamical climbing analogous to the ubiquitous Spring-Loaded Inverted Pendulum (SLIP) model (Cavagna et al. 1977; McMahon and Cheng 1990; Blickhan and Full 1993) in sagittal-plane, level-ground runners and the Lateral-Leg Spring (LLS) model (Schmitt and Holmes 2000) in sprawled, level-ground, lateral-plane runners. In

[1]GRASP Laboratory, University of Pennsylvania, Department of Electrical and Systems Engineering, Philadelphia, PA, USA
[2]Department of Mechanical Engineering, FAMU-FSU College of Engineering, Tallahassee, FL, USA
[3]Department of Mechanical Engineering, National Taiwan University, Taipei, Taiwan

Corresponding author:
Jonathan E Clark, Department of Mechanical Engineering, FAMU-FSU College of Engineering, 2525 Pottsdamer Street A-229, Tallahassee, FL, 32310, USA.
Email: clarkj@eng.fsu.edu

this paper, we explore the applicability of this new biological climbing template to the domain of robotics. We aim to build a fast, agile climbing robot capable of dynamical operation across a broad variety of scansorial environments, and we wish to test the proposition that adapting this biological template will prove both viable and effective to that end. This paper takes a step toward doing so by introducing a low degree of freedom electromechanical design that instantiates the template and exhibits dynamical climbing. In addition we present, a family of mathematical models used to inform and guide this design, which pursue scaling arguments and actuation analyses to draw the abstract animal template (Goldman et al. 2006) toward viable realization as a functional robotic platform.

Since the initial presentation of our biologically inspired dynamic climber (Clark et al. 2007), a number of other platforms have been developed that also explicitly exploit their dynamics in climbing, including: DynaClimber, which braces against parallel vertical walls to generate dynamic upward locomotion (Degani et al. 2007, 2011), RiSE v3, which ascends cylindrical vertical surfaces rapidly (up to 22 cm/s) using a pseudo-bound gait (Haynes et al. 2009), and ROCR, a T-shaped climber which ascends by exciting a pendular rotation using an actuated tail (Provancher et al. 2011). While the diverseness of these designs clearly indicates the interest in, and potential utility of, dynamic climbing, the platform herein offers several advantages that stem from the biological inspiration behind our work. These include: animal-like climbing speeds (over one body-length per second), rapid recovery from missed footholds, and the prospect for systematic comparison with and gradual incorporation of accumulating features of animal climbing. Chief among these intriguing future directions of inquiry are: (i) the role of sprawled attachment; (ii) the consequent prominence of lateral forces in dynamic climbing; and (iii) the coordination of level-to-vertical transitions in dynamical locomotion.[2]

The paper is organized in the following manner. Section 2 reviews the motivating bioinspiration, presenting the original Full–Goldman template (Goldman et al. 2006) and recounting its origins in animal climbing studies. Section 3 motivates and uses scaling arguments to explore the consequences of an order of magnitude increase in length. This increase arises from our aim to produce an engineered solution that might be realized as a utilitarian robot in the near term using present commercially available components. However, the Full–Goldman template, when scaled up to the prescribed utilitarian mass and length, entails a power density beyond the range of contemporary commercial actuators.

We consider this problem in Section 4 and implement modifications to the physical design, through the use of passive elastic energy storage to mitigate peak forces, and to the control scheme, by abandoning a prescribed length controller and adopting a power maximizing one to improve energy utilization. To allay the worry that these new active sources of dynamics might not be stable, Section 5 presents a study of their simplest useful mathematical representations. Namely we verify the stability of the vertical power stroke (the elastic member in parallel with a power maximizing controller) and the limb coordination controller (the scheme used to keep the limbs out of phase in the absence of a prescribed reference), both in isolation.

Informed by these numerical and mathematical analyses, we proceed in Section 6 to relate their impact upon the physical implementation and document its efficacy by presenting data obtained from a series of climbing experiments. An initial design yielded a working version of the template inspired climber: historically, the first dynamical vertical climbing robot. We further document how design modifications allow the prototype to climb at speeds dynamically similar to the Full–Goldman template. We conclude in Section 7 by commenting on some of the broader issues associated with robot climbers and discuss future work including limb coupling dynamics, energetics, stability, and adaptation to a more utilitarian polypedal morphology.

2. Biological origins of the climbing template

Organisms as diverse as arthropods and reptiles use differing limb number, attachment mechanism and body morphology to locomote on vertical substrates in a manner that rivals level ground running. Hence, it is natural to anticipate that diverse animals would develop correspondingly divergent climbing strategies. Surprisingly, Goldman et al. (2006) have discovered common dynamics in extremely different rapidly climbing organisms (cockroaches and geckos). Perhaps equally unexpected, neither climbs straight up a vertical surface. Both organisms generate large, inward lateral forces during climbs over 4 body-lengths per second that produce substantial changes in lateral, as well as fore–aft, velocity (Autumn et al. 2006; Goldman et al. 2006).

A model which generates the template dynamics of vertical climbing is shown in Figure 1(A) and a time-lapse picture of its motion in Figure 1(B). The model consists of a rigid body that is pulled upward and side-to-side through the action of a spring in series with a linear actuator.

As shown in Figure 1, the first step with the right leg begins at touchdown, with the right actuator maximally extended, and the spring relaxed with zero rest length. Touchdown coincides with the establishment of a rotationally free pin joint between the foot and the wall. As the actuator length $L(t)$ decreases, the leg spring extends, the foot freely pivots about the point of contact and the center of mass (COM) is translated vertically and laterally. The right foot maintains attachment with the wall until the leg actuator has reached maximum compression, following which the left leg touches down and the process repeats for that leg. The actuator changes length sinusoidally such that

$$L(t) = \frac{l_s}{2}(1 + \sin(2\pi ft)) + L_0, \tag{1}$$

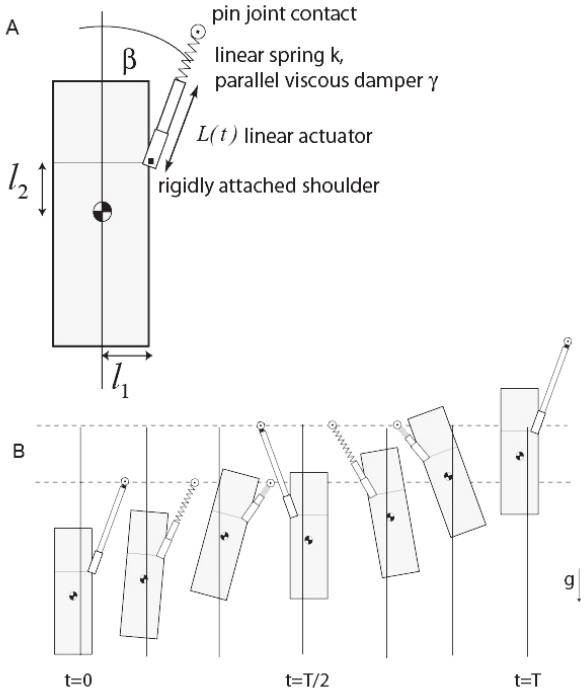

Fig. 1. The Full–Goldman (FG) dynamic template for climbing, with g as the direction of gravity. This two-degree-of-freedom model generates the template climbing dynamics shown in Figure 2(C). (A) Schematic of the model. (B) Schematic of the motion of the model during two steps. The extension of the spring has been exaggerated for clarity. (Reproduced with permission from Goldman et al. (2006).)

where l_s is the step length, L_0 is the retracted length of the leg, f is the stride frequency, and t is the time since the most recent touchdown was established. The solid vertical line in each panel indicates the fixed lateral position about which the center of mass laterally oscillates. The angular excursion of the body and extension of the spring are exaggerated for clarity. Actual angular excursion of the body relative to vertical is approximately $\pm 3^\circ$.[3] The model was coded and integrated in the Working Model 2D (Design Simulation Technologies, Inc.) simulation environment.

The forces and resulting COM velocities generated by this position-based control of the actuators in the model are shown in Figure 2 and agree well with the published patterns measured in cockroaches and geckos (Goldman et al. 2006). The representative magnitude and phasing of forces and center of mass velocities was found after systematic variation of system parameters.[4]

We now proceed to discuss the sequence of design and control choices leading to the construction of a robot that anchors this template.[5]

3. Scaling of the template

While the Full–Goldman template was designed to describe the dynamical climbing motions of 2 g animals, present day climbing robots that have achieved (Balaguer et al. 2000; La Rosa et al. 2002; Provancher et al. 2011) or are close (Bretl et al. 2003; Xiao et al. 2005; Spenko et al. 2008) to utilitarian realization are all several (two or three) orders of magnitude larger. More pragmatically, only recently have novel technologies emerged permitting the construction of legged robots at a small (1–10 g) scale (e.g. Birkmeyer et al. (2009) present a 16 g legged runner). To build a dynamical climbing platform at this scale, we would have to rely on remote-control operation (as did Birkmeyer et al. 2009), eliminating the capacity for autonomous operation. Moreover, we expect near-term dynamical climbers to be faced with complex terrain navigation decisions which mandate on-board intelligence.

Given the contemporary prevalence of kilogram-scale climbing machines and the difficulties of constructing a robot at the template's 2 g mass, we instead scale the physical parameters of the template to arrive at a climbing model which demonstrates dynamically similar climbing behavior with a more easily realizable size and mass. With a target mass of 2 kg, we shift attention to the question of scaling, emphasizing what we mean by dynamically similar behavior and how it can be achieved. Guided by Alexander and Jayes (1983), we adopt a definition of 'dynamic similarity' that designates two motions to be dynamically similar if all lengths, times, and forces are scaled by simple scaling factors that preserve the non-dimensional properties, such as Froude and Strouhal numbers. This implies that dynamically similar systems produce similar dynamic motions and guarantees the preservation of stability properties regardless of scale (Schmitt et al. 2002).

With dynamical similarity defined, we now determine the scale factors which expand the 2 g template into a 2 kg, dynamically similar variant. For the purposes of this investigation, length, scaled by α_L, is taken to be the base property from which other scale ratios are computed. We assume that the mass scaling ratio α_M varies as the cube of length to preserve material density. Since a 1,000-fold increase in mass is desired,

$$\alpha_M =: \alpha_L^3 = 1{,}000, \tag{2}$$

from which $\alpha_L = 10$. Recalling that rotational inertia I for a point mass m a distance r from the pivot point is $m \cdot r^2$, the scaled template's rotational inertia is, as a result of the length and mass scaling, increased by a factor of

$$\alpha_I =: \alpha_M \cdot \alpha_L^2 = \alpha_L^5 = 10^5. \tag{3}$$

The scaling for the natural frequency of the body α_ω can be found by examining the pendular motion of the model. The climber's body rotates about a pinned stance foot with a frequency of $\frac{1}{2\pi}\sqrt{\frac{m \cdot g \cdot r}{I}}$, where g is gravity. Plugging in the known scale factors for these parameters, we find that the natural frequency of the body scales as

$$\alpha_\omega =: \sqrt{\frac{\alpha_M \cdot \alpha_L}{\alpha_I}} = \alpha_L^{-\frac{1}{2}} = 0.316. \tag{4}$$

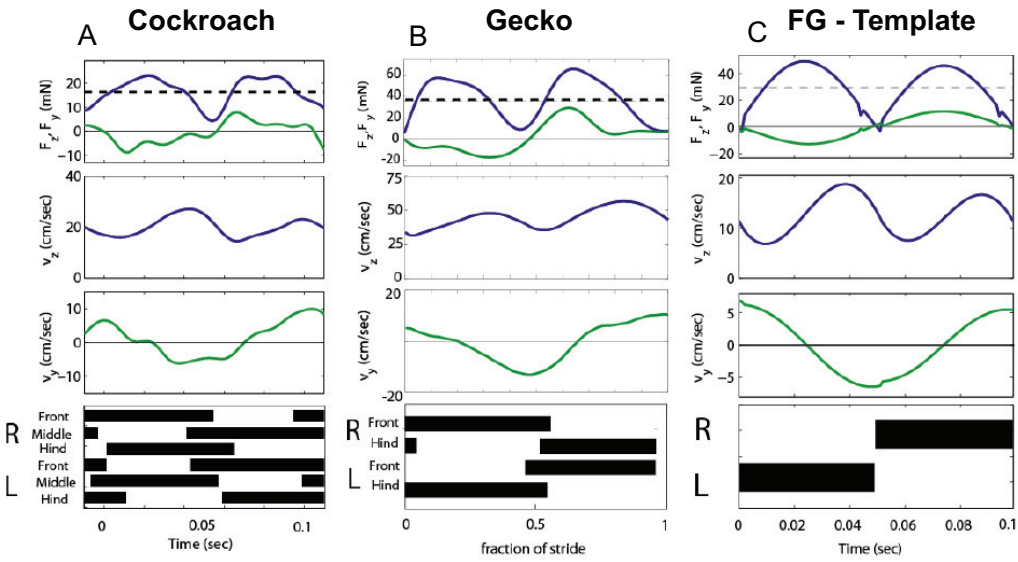

Fig. 2. Force (vertical F_z and lateral F_y), vertical velocity (V_z), lateral velocity (V_y), and foot fall patterns for the cockroach, gecko, and Full–Goldman template. Broken lines indicate body weight. Data are shown for a normalized stride, with black bars representing foot contact. (Reproduced with permission from (Goldman et al. 2006).)

The preservation of frequency ratios requires us to scale both the pendular and the vibrational frequency by the same factor. The pendular frequency is also proportional to the leg driving frequency, which is established by a controller and has no immediate physical design consequences; we simply reduce the driven frequency from 9 Hz (which was observed in cockroaches (Goldman et al. 2006)) to 2.85 Hz. To maintain the proper vibrational frequency, the wrist spring must be appropriately scaled. The natural of the frequency of the spring with stiffness k is given by $\frac{1}{2\pi}\sqrt{\frac{k}{m}}$. Since the vibrational frequency scales by the same ratio as pendular frequency, the scaling factor of the spring is given by

$$\alpha_k =: \alpha_M \cdot \alpha_\omega^2 = \alpha_L^2 = 100. \tag{5}$$

The final physical parameter scaling ratio which must be determined is damping b, exhibited in the model in the wrist damper. Since the force due to damping F_b can be written as $v \cdot b$, where v is velocity, ratios must first be determined for both force and velocity. Using the general expressions for each ($F = m \cdot a$ and $v = m/s$), the scaling factor for force and velocity are

$$\alpha_F =: \alpha_M \cdot \alpha_L \cdot \alpha_\omega^2 = \alpha_L^3 = 1{,}000, \tag{6}$$

and

$$\alpha_V =: \alpha_L \cdot \alpha_\omega = \alpha_L^{-\frac{1}{2}} = 0.316. \tag{7}$$

The damping scaling factor can then be written as

$$\alpha_b =: \frac{\alpha_F}{\alpha_V} = \alpha_L^{\frac{5}{2}} = 316. \tag{8}$$

These scaling factors can be checked to ensure that the non-dimensional parameters are conserved appropriately. The Froude number, given as $Fr =: v^2/g \cdot l$, is constant since both v^2 and $g \cdot l$ scale as a factor of α_L. Likewise, the Strouhal number, given as $Fr =: \omega \cdot l/v$, is constant as both $\omega \cdot l$ and v scale proportional to $\alpha_L^{-\frac{1}{2}}$.[6] Thus, these scaling ratios will allow for dynamic similarity to be maintained as the template is scaled. Note that dynamic similarity does not necessarily guarantee the preservation of other (scale dependent) performance metrics. For example, if we calculate speed using body-lengths per second (bl/s), the original template climbs at 4.5 bl/s, while its scaled variant climbs at only 1.4 bl/s.[7]

Figure 3 presents the ground reaction forces and COM velocities over one stride at steady state, illustrating the effect of scaling on the dynamic behavior under the scaling laws proposed above. The phasing of body motions and forces has been preserved, and the magnitude of the scaled template's velocity and ground reaction force matches the prediction.

One consideration not accounted for above is the issue of available power for dynamical climbing. Biological actuators (muscles) differ from and are in many ways superior to current commercially available prime movers (Rome et al. 1988; Kornbluh et al. 1998). A major limitation of commercially available actuation technology is the scaling of power density. Using the scaling ratios, the corresponding increase in power density with scale can be determined:

$$\alpha_{\frac{power}{weight}} = \frac{\alpha_F \cdot \alpha_V}{\alpha_M} = \alpha_L^{\frac{1}{2}} = 3.16. \tag{9}$$

The increase required in power density has an intuitive explanation. With no energy sinks, vertical climbing speed is given by $\frac{\text{power}}{\text{force}}$, and at a constant velocity, the force applied

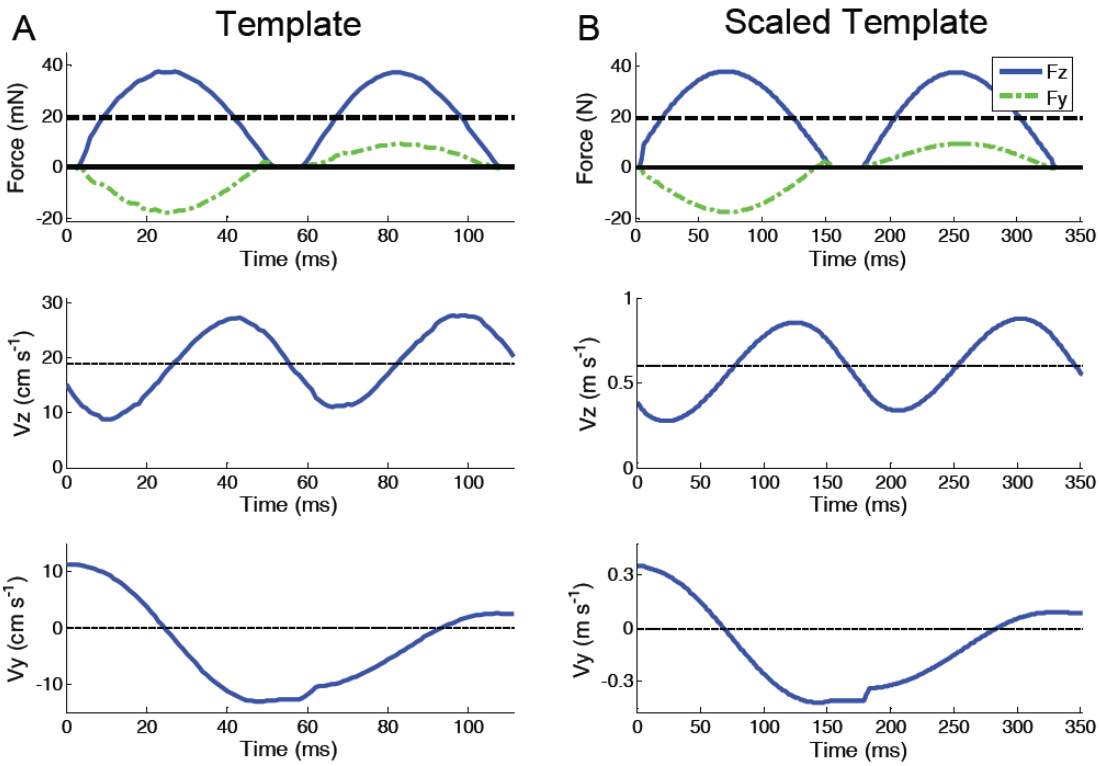

Fig. 3. Force(vertical F_z and lateral F_y), vertical velocity (V_z), and lateral velocity (V_y) for the animal template model and the scaled robot template. The heavy dashed horizontal lines represent the weight of the robot and the light dashed lines are the mean velocities. Note the change in units for the scaled template.

is equal to the climber's weight. Thus, if the desired velocity increases, as it must to maintain dynamic similarity, the climber's power-to-weight ratio must increase correspondingly. However, conventional actuators tend to maintain a constant power density, regardless of scale. While we have chosen to restrict attention to conventionally amplified and driven brushed DC motors, our experience, corroborated by the discussion of Hollerbach et al. (1992), is that all available alternatives can, at best, offer similar power density.

The reported power densities achieved in prior climbing and running robots varies greatly, but as a point of reference, both the hexapedal RiSE (Autumn et al. 2005) and RHex (Altendorfer et al. 2001) robots have a specific power of about 10 W/kg per tripod. Simulations at the original scale predict that each of the template's legs (each template leg is the equivalent of a tripod of cockroach legs) must achieve a peak power output of 6.3 W/kg. However, scaling the climber's length by an order of magnitude increases the power demand by a factor of 3.16 to 20 W/kg per leg. Given that actuators demand, at peak load, roughly twice the power endowment of previous legged robotic platforms, there are several potential solutions: improve the actuators' power density; reduce the peak power load; or settle for slower speeds. As described in Section 4, we pursue the second course.

4. Model design alterations for realizability

To build DynoClimber, a robot which anchors the Full–Goldman template, we must modify the template's mass distribution, power transmission design, and approach to limb control. In this section we derive and discuss each of these changes with heavy reliance on simulation as a design tool.

4.1. Mass distribution and linkage design

To generate linear foot motion with a standard brushed rotational electric motor,[8] we must build a transmission mechanism. Here we utilize a simple crank–slider mechanism (similar to the piston/crank used in automobile engines), as shown in Figure 4. A principal advantage of this design is the unidirectional motor operation; the robot's motors do not need to change direction to reverse the direction of the feet.

To account for the mass of the attachment mechanism and transmission, we distribute some of the simulated climber's body mass to the legs. The total mass and footprint of the climber remains unchanged. A lateral degree of freedom and lateral compliance have been added to each of the hips to remove the kinematic singularity associated with double support phase. The stiffness and damping of

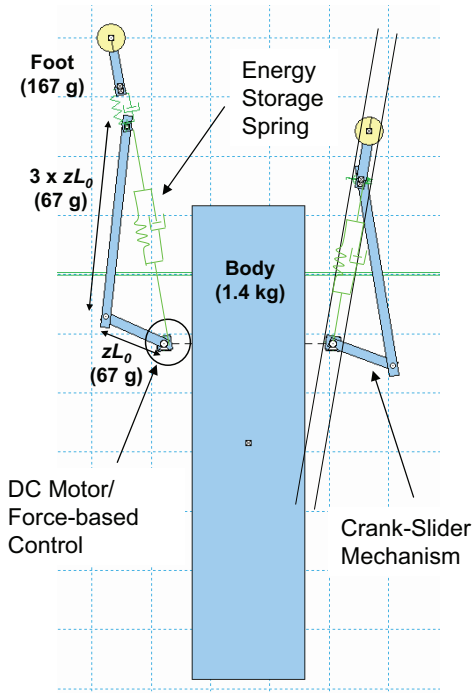

Fig. 4. Schematic of the crank–slider mechanism used to convert rotary (motor) output into linear motion. The relative lengths and masses of the links are indicated.

these new lateral hips are set equal in magnitude to the wrist springs, but since they are typically orthogonal to gravity, their deflection primarily occurs when both legs are attempting to simultaneously contract during incidental double support phases during the startup transient.

4.2. Power limitations

As described in Section 3, the power density required for a 2 kg bipedal dynamic climber, 20 W/kg per leg, is double the power density achieved by former legged robots. Worse, preliminary simulations of a 2 kg crank–slider equipped climber indicate that the peak mechanical power output required from each motor exceeds 40 W.

Two prospective changes, shortening the stride length or decreasing the climbing frequency, prove effective in terms of reducing peak power, but affect the dynamics of climbing severely, reducing climbing speed to 10–25% of the scaled template velocity. Other, less dynamically disruptive choices include operating the motors with an accumulating 'thermal debt', and mechanically coupling the robot's limbs.

The motors may be 'overrun' for short periods at the expense of producing more heat than can be dissipated. Thus, 'thermal borrowing' can be used for short periods if the mean power draw is low enough. For a vertical climber, however, power requirements are large and roughly constant, reducing the relevance of intermittent operation.[9]

If the legs of the robot must only deliver maximum power during intermittent intervals (in this case, each leg's stance phase) and these intervals are phase offset from one another, a single, more powerful motor could be used to drive multiple mechanically coupled multiple joints or limbs. While the peak power draw would not decrease, a larger motor might be able to supply this power output without overheating. iSprawl (Kim et al. 2006), MechaRoach (Boggess et al. 2004), and several toy robots have employed this approach. However, this imposes rigidly fixed leg trajectories which would not allow investigation of other behaviors and controllers, hindering the development of a more versatile climber.

In order to maintain individual control of the legs and simultaneously overcome the power limitation of commercial motors, we utilize passive–elastic elements in parallel with the leg actuators. As suggested by the simplified numerical studies of Clark and Koditschek (2006), this method allows the legs to store energy during the swing-recirculation phase of their motion, while the power requirement is low, and then release the energy during stance to aid with accelerating the body upwards.

With the addition of these legs springs the peak power required for each leg drops to just over 20 W during steady-state climbing. Since the velocities of the cranks are unchanged, the locomotion dynamics of the system remain the same as without the spring.

While this strategy solves the power problem during the steady-state climbing, a peak power output of more than 40 W is still required to accelerate the robot from rest. To better handle transient acceleration, a robot will require a more adaptive and efficient control scheme than the prescribed constant angular velocity scheme utilized for the animal template. A preliminary approach, described below, was utilized in the design simulation, and a more refined version of this idea was implemented in the robot as described in Section 5.2.

4.3. Force controlled actuation

To better exploit the robot's available on-board power, we switch from commanding positions to commanding force, at least up to the actuators' abilities to deliver it. By explicitly regulating the motors' outputs rather than relying on position tracking errors, the actuators can be used to produce a greater amount of positive work during a stride. At the same time, this control framework sidesteps the need to design different reference motions for the vastly different operating regimes the robot encounters on its transient from standstill to steady state. Controlling them, instead, to extract the greatest possible amount of work against gravity regardless of operating regime enables the actuators to build up body COM speed over a number of strides, in an autonomous manner more naturally suited to the range of transient conditions encountered along the way.

A new issue arising from the introduction of the force-maximization controller is the challenge of ensuring the proper anti-phase coordination of legs. An earlier analytical

study of coupled oscillatory climbing systems has shown that the limbs of these systems naturally phase lock, resulting in extremely large double support and aerial phases (Komsuoglu 2004).

The switch from a trajectory-tracking to a force-based control scheme also results in a relinquishment of our control of the overall actuation frequency. While this frequency shifting during climbing can increase the performance of the robot, it also complicates the dynamic coupling between the leg switching, body rotation, and wrist-spring extension by introducing additional actuator dynamics. Concerns about potentially adverse dynamical interactions are addressed in the next section.

4.4. Simulation conclusions

The net result of the design alterations described in this section is a realistically sized and powered dynamic climber that performs in a manner similar to the template derived from animal studies. The robot's projected vertical speed of 0.55 m/s compares very favorably to that of the scaled template (0.60 m/s). The addition of a force-assist spring in parallel with the actuator in the legs and the switch to a force-maximizing control scheme allow a simulated robot to climb dynamically at our target mass of 2 kg while reducing the peak power load by almost 50%.

According to (9), a climber's power-to-weight ratio must increase as the square root of length to preserve dynamic similarity. Thus, any increase in size requires an increase in power density. Since DynoClimber, when equipped with passive–elastic energy storage and an aggressive force-maximizing controller, is just able to achieve the power density required to climb dynamically, a substantial increase in size would mandate that the robot achieve an unrealizable power density. As described in Section 4.2, attempting to climb when underpowered has a severe effect on upward speed. Thus, it appears that with our present motor power density and control scheme this anchor approaches the upper limit on speed at near-term utilitarian length scales for the Full–Goldman template.

5. Stability of the internal climber dynamics

Simulations presented in Goldman et al. (2006) indicate that the Full–Goldman template converges to and climbs with a stable, period-one gait. The template's prescribed leg-length actuation scheme (described by (1)) rigidly dictates leg frequency and therefore makes asymmetrical or irregular gaits unlikely to appear. However, to anchor the template in a robot, the previous section has introduced two proposed changes to the template's actuation scheme. First, in Section 4.2, we introduce parallel energy-storage springs to reduce the (peak) power density required for dynamic climbing, and second, in Section 4.3, we equip the proposed mechanism with a control policy that permits us to maximize actuator power output (losing precise specification of leg frequency).

By design, our controller causes the climber's motors to operate along their speed–torque curve, and therefore exposes it to the motors' dynamics, speed/force trade-off, and inherent power limitations; the parallel spring introduces yet another dynamical exchange of potential and kinetic energy. The addition of these dynamics raises a concern that the coupled electromechanical plant may exhibit unstable or unfavorable oscillations which do not appear in the template. While our design simulation appears to climb without spurious effects caused by these modifications, through simulation alone we are unable to comprehensively assess the robustness of the climber's behavior to parameter or initial condition variations.

In this section we formalize the foregoing design models, simplifying and decoupling them to the extent that mathematical guarantees can be established precluding the possibility of such undesired dynamical instabilities over any initial conditions for any physically reasonable choice of design parameters. We first consider the vertical power stroke in isolation from the leg alternation dynamics and give a proof that a simplified one-degree-of-freedom abstraction of the resulting dynamical system is globally asymptotically stable. We next introduce a more parametrically parsimonious (yet still analytically tractable) phase regulation controller and give a proof that our phase alternation dynamics, in isolation from the mechanical power stroke dynamics is also globally asymptotically stable.

5.1. Power stroke modeling and analysis

The Full–Goldman template's counterparts for level ground running, the SLIP and LLS templates, have generated a more-than-decade long literature (Holmes et al. 2006) and remain an active area of research in legged locomotion. Early analysis (Kodistchek and Buehler 1991) of the first dynamical running machines (Raibert 1986) demonstrated that a poorly tuned actuation subsystem could be responsible for the period-two (or higher) 'limping gaits' observed in vertical hopping (Kodistchek and Buehler 1991) and juggling (Buehler et al. 1994). Even the simplest two-degree-of-freedom model of the unactuated SLIP templates displays higher-order (period-two) limping gaits in a physically relevant parameter regime (Ghigliazza et al. 2005). It is notable, then, that the design simulation does not seem to exhibit period-two gaits. Thus, two factors contribute to our motivation to undertake at least a rudimentary analysis of our climber's stability: our introduction of actuator dynamics, and the precedence of higher-period gaits in prior locomotion templates.

In the tradition of that past literature we introduce in this first analysis of the DynoClimber design prototype the simplest model that can still capture the crucial interaction of mass and motor dynamics: a one-degree-of-freedom representation of our climber's 'power train', the dynamics of

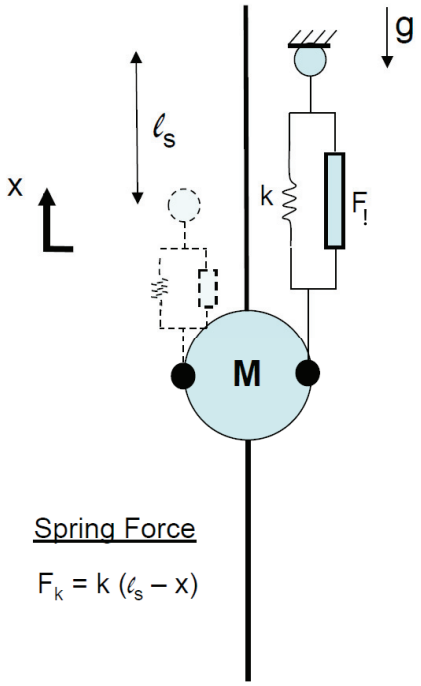

Fig. 5. Schematic of the climbing model used. The spring is fully loaded when the leg reaches full extension.

force-actuated vertical climbing, independent of rotational dynamics.[10] To that end, we build a simplified mathematical model composed of a point mass propelled vertically upward by an actuator.

When instantiated with a range of physically motivated parameter values that includes those characterizing our particular robot prototypes, this vertical power stroke model converges to a period-one gait from all initial conditions as we now show. While not a conclusive statement as to the stability of the physical coupled system, this result demonstrates that the power stroke dynamics cannot in and of themselves be a source of instability or parasitic, higher-period dynamics.

5.1.1. Vertical power stroke model As depicted in Figure 5, the vertical power stroke model consists of a rigid body of mass M and two massless legs operating in a one-dimensional workspace, the climbing 'wire', subject at all times to a constant gravitational force $M \cdot g$. By construction, exactly one foot is attached, and applying force, to the substrate at all times. Since the feet are massless, the unattached foot does not affect the climber's upward progress.

A foot begins its stance phase by attaching to a fixed point on the substrate with its corresponding leg extended to the full stride length, l_s. That leg applies a contractile force (described in detail in the next paragraph) propelling the climber's mass upward. When the mass has traveled a vertical distance upward of l_s, the foot in contact with the wall instantaneously breaks contact, while the other foot simultaneously establishes contact, once again at a distance of l_s from the mass.

The stance-phase contractile force consists of two elements intended to resemble the transmission used in ours design simulation: an energy-storage spring with Hooke law constant k in parallel with a motor-based force F_m. The energy storage spring begins each stride producing maximal upward force, $l_s \cdot k$. That force diminishes throughout the stride until the stride terminates with the spring at its rest length, producing a force of zero. The motor-based force is given by a motor and gearbox driving a simulated rack and pinion transmission mechanism. We approximate the physical transmission, a crank slider, by an ideal rack and pinion to promote analytical tractability.

The motor produces a rotational torque which is amplified linearly by the gearbox with gear ratio G. This force drives the simulated pinion (with radius r) which proportionately converts the torque from the gearbox to a linear force. Thus, a motor torque τ_m produces a prismatic output force of $F_m = \frac{G}{r} \cdot \tau_m$.

The control scheme is as simple as possible: the stance leg's motor is assigned a constant voltage at all times. We demonstrate in Section 6.1.1 that this scheme results in identical steady-state behavior to the controller in Section 4.3, but requires less electrical and software infrastructure to implement. At a speed of zero, the motor produces its full stall torque of τ_s, and motor torque production decreases linearly with motor speed until the motor produces a torque of zero at its no-load speed ω_{nl}, as per the standard linear motor model (Gregorio et al. 1997).[11] It bears noting that τ_s and ω_{nl} are given for a nominal voltage; changing the voltage applied to the motor scales each of these terms linearly.

The parameters used to define the vertical power stroke model are summarized in Table 3. Note that throughout this section, we rarely refer to torques and angular speeds, preferring the equivalent linear forces and velocities.

Figure 6 introduces the coordinates $z = (z_1, z_2) = (z, \dot{z}) \in \mathcal{Z} =: \mathbb{R}^2$ and depicts the physically relevant state space of the climbing model. This is a rectangle in the upper half plane bounded by the abscissa below, $\mathcal{L}_2$, indicating an upward velocity of zero, and two vertical lines, the demarcation of kinematic limits. The ordinate to the left, $\mathcal{L}_1$, at $z_1 = 0$, and a parallel line, $\tilde{\mathcal{L}}_1$, to the right, at $z_1 = l_s$ bound the physically permitted stroke length and extension of the spring. When the system trajectory intersects $\tilde{\mathcal{L}}_1$, the reset function s is applied and a new stride begins with the system trajectory lying along $\mathcal{L}_1$ with the same coordinate value as before. This reset map, s, is depicted in Figure 6: it corresponds to the termination of one leg's stance phase and simultaneous attachment of the other leg to the wall.

Using $z \in \mathcal{Z}$ coordinates, the equations of motion for the body, with mass M, can be written by inspection from Figure 5 as

$$\dot{z_1} = z_2$$

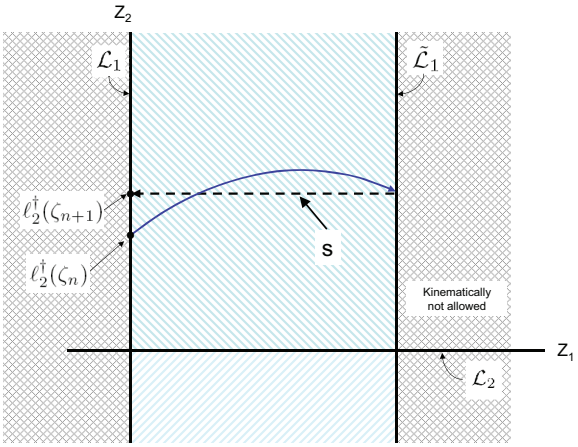

Fig. 6. Patches, boundary sets, and sample trajectory from initial condition ζ_n on $\mathcal{L}_1$ to $\tilde{\mathcal{L}}_1$, then projected back onto $\mathcal{L}_1$, via the reset function s, to represent the next iterate under the return map, ζ_{n+1} for the simplified climber.

$$M\dot{z_2} = F_k + F_m - Mg$$

where the spring force is $F_k =: k(l_s - z_1)$, and the motor force is

$$F_m =: F_s \cdot (1 - \frac{z_2}{v_{nl}}), \tag{10}$$

where F_s is the stall force of the motor. The resulting second-order dynamics are given by

$$\dot{z} = Az + b \tag{11}$$

with

$$A = \begin{bmatrix} 0 & 1 \\ -\alpha^2 & -2 \cdot \sigma \cdot \alpha \end{bmatrix}, b = \begin{bmatrix} 0 \\ \beta \end{bmatrix},$$

where the terms used in (11) are summarized in Table 1.

5.1.2. Return map As is standard, our analysis focuses on the discrete time iterates of a return map (Guckenheimer and Holmes 1983). In this case, the velocity of the climbing mass is sampled at an event (the 'section') which is revisited again and again as the robot climbs. The section employed here is the touchdown of the next extended limb; this occurs when a system trajectory intersects $\tilde{\mathcal{L}}_1$ and the reset function s is applied. By examining the velocity of the climber at the beginning of each stride, we demonstrate analytically that it converges to a period-one gait.

We write the return map, R, using section coordinates $\zeta \in \mathcal{L}_1$, as depicted in Figure 6. This scalar variable, ζ, represents physically the climber's vertical velocity at the start of a stride. Trajectories arise as the composition of the flow from $\mathcal{L}_1$ to $\tilde{\mathcal{L}}_1$ with a 'swing resetting event' (s) that maps the body state associated with a completely compressed arm at a given velocity in $\tilde{\mathcal{L}}_1$ to the same body state associated with a completely extended (contralateral) arm at the same velocity in $\mathcal{L}_1$. The reset function s that formalizes this swing resetting event can now be written down directly as

$$s(z_1, z_2) := (0, z_2).$$

We denote by the symbol $f^t(z)$, the time trajectory of the dynamics (11) through some initial condition, z. We also define the projection operators $\ell_1(z_1, z_2) := z_1$ and $\ell_2(z_1, z_2) := z_2$, as well as the pseudo-inverse $\ell_2^\dagger(z_2) := (0, z_2)$ Because we are interested in initial conditions on the section, $\mathcal{L}_1$, we parameterize these trajectories by $\zeta \in \mathbb{R}$ via composition with $\ell_2^\dagger$ and ℓ_2. Using these functions, we define the return map, $R := \ell_2 \circ s \circ f^T \circ \ell_2^\dagger(\zeta)$, where T is the time taken to the end of the stride.

Here R quantifies how the system evolves from the beginning of one step to the beginning of the next. It is composed of the flow induced by the vector field (11) and the reset function s. Details of the derivation of the return map can be found in Appendix A. The return map can be expressed as

$$R(\zeta) = \frac{1}{2\alpha\sqrt{\sigma^2 - 1}} * \left(\lambda_1 e^{\alpha\lambda_1 T}[\beta\lambda_2 + \alpha\zeta] - \lambda_2 e^{\alpha\lambda_2 T}[\beta\lambda_1 + \alpha\zeta]\right). \tag{12}$$

Note that T is defined implicitly as a function of ζ (see Appendix A for a careful definition), making a closed-form solution of the return map impossible. However, we are able to investigate the stability properties of the return map by examining its derivative, DR, derived in the appendix, and written in more compact form as

$$DR(\zeta) = \frac{(2\rho d)(e^{-\alpha\sigma T})}{\rho(d^2 + 1) + c(d^2 - 1)}, \tag{13}$$

where for ease of analysis we introduce the following substitutions:

$$\rho(\zeta) := \zeta\alpha\sqrt{\sigma^2 - 1} \tag{14}$$

$$c(\zeta) := \beta - \alpha\sigma\zeta \tag{15}$$

$$d(\zeta) := e^{T\rho(\zeta)/\zeta}. \tag{16}$$

5.1.3. Physically imposed flow boundaries To analyze the properties of the flow precisely we examine the acceleration null-cline (zeros of the acceleration component of the vector fields) located on the affine set:

$$\mathcal{N} := \{(z_1, z_2) \in \mathbb{R}^2 \mid z_2 = \frac{\beta}{2\sigma\alpha} - z_1 \cdot \frac{\alpha}{2\sigma}\}.$$

This defines a region below $\mathcal{N}$, as depicted by the '+' sign in Figure 7, within which the trajectory experiences an increase in vertical velocity due to the accelerating effects of the actuator and spring. We find it useful to impose a partition of the section $\mathcal{L}_1$ by labeling the special point where it intersects the null-cline,

$$\zeta_B := \ell_2(\mathcal{N} \cap \mathcal{L}_1). \tag{17}$$

Table 1. Elements of the equations of motion.

Term	Definition	Physical Meaning
α	$\sqrt{\frac{k}{M}}$	Natural spring–mass frequency
σ	$\frac{F_s}{2 \cdot M \cdot v_{nl} \cdot \alpha}$	Effective damping due to motor back-EMF
β	$\frac{1}{M}(-M \cdot g + k \cdot l_s + F_s)$	Net vertical force at stall

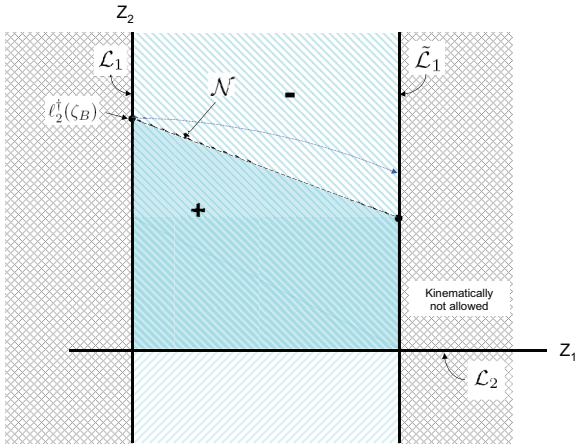

Fig. 7. The null-cline of the system ($\mathcal{N}$) overlaid on the patches and boundary sets of the system. For states above and to the right of the null-clines the vector field is increasing (indicated by the '+' signs), and beneath and to the left the vector field is decreasing (indicated by '−' signs).

Beginning with this initial condition, a climber's spring and motor together provide just enough force to support its mass at the beginning of the stride. In the proof that follows we observe that trajectories initiating with this and all larger velocities remain above the null-cline and hence experience decreasing vertical velocity throughout the stride.

5.1.4. Proof of stability We now demonstrate that the climber's return map has a globally asymptotically stable fixed point, meaning that from every initial condition the climber converges to a stable period-one gait. The proof entails establishing three claims:

(a) The return map R has a slope between zero and one over interval $I = [0, \zeta_B]$.
(b) The inertia I is invariant under R; in addition, I is attractive from above.
(c) Starting from any initial velocity $\zeta_0 \geq 0$, iterates of the return map converge to a unique fixed point:

$$\lim_{n \to \infty} R^n(\zeta_0) = \zeta^*.$$

The details of the proof are presented in Appendix B.

5.1.5. Summary discussion of the power stroke model analysis Our power stroke model, if equipped with parameters within the physically relevant range introduced in Table 5, converges to a steady-state, non-limping gait, represented by the return map fixed point, ζ^* determined in Proposition 4 in Appendix B and representative of the physical average climbing velocity

$$\bar{\zeta}^* := \frac{1}{T} \int_0^T \ell_2 \circ f^t \circ \tilde{\ell}_2(\zeta^*)\, dt. \tag{18}$$

Thus, the introduction of an actuator model equipped power stroke does not itself introduce instability.

This analysis of a simplified one-dimensional model has utility in terms of understanding the underlying dynamics of climbing, and in informing future design decisions. It has been shown that for parameter ranges that correspond to robot designs of interest the dynamics of this hybrid system in the vertical direction are naturally self-stabilizing. This global stability behavior exists notwithstanding the absence of mechanical damping. Instead, motor back-EMF acts as a damper, monotonically reducing motor force as a function of the climber's vertical speed.

In ongoing work, we are investigating the stability properties of a more general class of climbing dynamics models. For purposes of the present paper, however, this analysis supports the conclusion that the use of passive energy storage elements to distribute the load on the actuator over a wider percentage of the cycle results in faster climbing without adversely affecting the vertical stability of our particular climber. With confidence in the underlying dynamic properties we can proceed with the construction and physical testing of the physical power train.

5.2. Coordination controllers

With the introduction of a force-based control scheme, as discussed in Section 4.3, a leg coordination controller needs to be added to ensure proper out-of-phase operation of the legs during climbing. On the initial version of the robot a 'mirror-law'-based coordination controller was implemented. The inefficiency and fragility of this approach prompted the development of a force-maximizing, self-exciting controller described in Section 5.2.2.

5.2.1. Mirror law In a 'mirror-law' controller, first introduced by Buehler et al. (1990), a leg in stance mode is commanded the highest permissible voltage, $V_{\text{stance}} = V_{\max}$, while the leg in flight mode is controlled to follow the stance leg with an offset of π, namely

$$V_{\text{flight}} = k_p * (\theta_f - \theta_s - \pi) + k_d * (\dot{\theta}_f - \dot{\theta}_s) \tag{19}$$

where subtraction on the circle is done modulo 2π; k_p and k_d are controller gains, θ_f and θ_s are the positions of the leg in flight and stance respectively, and $\dot{\theta}_f$ and $\dot{\theta}_s$ are the corresponding velocities.

This control law results in empirical convergence to a limit cycle; unfortunately, it also abruptly slows each leg once every stride. The abruptness in behavior is a consequence of the controller's intrinsic non-smoothness originating in the hybrid transition between stance and flight mode.

In addition to slowing the robot's pace overall, the abrupt transitions required by the mirror-law controller result in substantial mechanical stress and electrical noise. Thus, complementing the robot's mechanical and electrical redesign (described in Section 6.1), we designed a controller which achieves the same goals as the mirror law without such abrupt transitions.

5.2.2. Self-exciting, work-directed With the goal of eliminating non-smooth controller transitions and ultimately improving climbing behavior, while achieving a greater degree of mathematical tractability, we introduce a new self-exciting, work-directed controller.

This controller, like its predecessor, employs a self-exciting (clock-free) approach but admits an analytical proof of stability, while obviating any need for gain tuning to ensure tracking (this proof is demonstrated in Section 5.3). The control law is written in terms of the commanded voltage signal $V =: (V_1, V_2)$ and the difference between the motor shaft angles $\Theta = (\theta_1, \theta_2)$, $\delta = \theta_1 - \theta_2$ where

$$V(\Theta) = V_{\max} \begin{bmatrix} 1 \\ 1 \end{bmatrix} - k_r \sin^2(\delta) \cdot \begin{bmatrix} \mathrm{u} \circ \sin(-\delta) \\ \mathrm{u} \circ \sin(\delta) \end{bmatrix} \quad (20)$$

where $V_{\max}$ is the maximum voltage and the unit step function, u, outputs the scalar value 1 if its argument is positive and outputs 0 elsewhere.

The retarding gain, k_r, determines the transient behavior of the system; a larger k_r forces the system to converge more quickly, at the expense of speed of oscillation during the transient period and any time the system is perturbed from its limit cycle. With a k_r near zero, on the other hand, the system will return more slowly to its limit cycle during any transient period, but both motors will, on average, be commanded higher voltages while the system is away from its limit behavior. As shown in the next section, regardless of the choice of k_r, the system provably converges to a limit cycle with a velocity which does not depend on the retarding gain. Moreover, as long as k_r is kept between zero and two, the controller will not exceed the specified maximum voltage, $V_{\max}$. For the experiments described in Section 6.4, k_r has been fixed equal to 0.5. With this value of k_r, the resulting vector field is displayed on the controller phase portrait is shown in Figure 8. This controller effectively implements hybrid transitions smoothly and in a provably correct way.

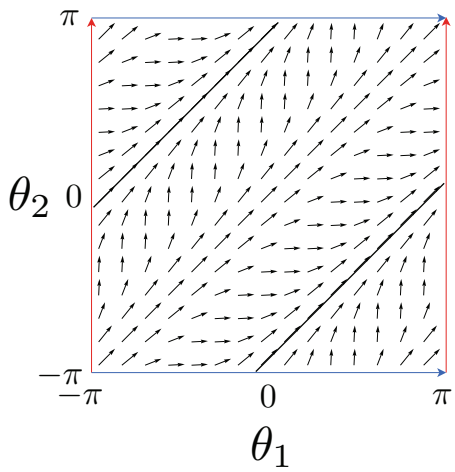

Fig. 8. Phase portrait of the control vector field. When θ_1 or θ_2 is less than zero, the corresponding leg is in flight. The solid diagonal lines represent the desired out-of-phase trajectory.

As shown in Section 6.4, this controller permits the robot to climb at an unprecedented pace and, anecdotally, substantially reduces the stress experienced by the robot's electrical and mechanical components.

5.3. Self-excited controller analysis

Given the empirical success of the self-exciting, work-directed controller, we now analyze its stability to be sure that it will accomplish the prescribed goals regardless of initial condition or parameter choices. Thus, in this section we prove the correctness of a class of self-exciting, work-directed controllers. One controller from that class was used for DynoClimber's most rapid climbing, and is presented in Section 5.2.2.

We first introduce a simplified leg-coordination model of the physical motor system in order to provide an analytical basis for the success of our controller. This model is not intended to be accurate to our specific robot. Instead, we construct a general actuator model and prove that our controller functions as desired if applied to any actuator chosen from that class (including, of course, the specific actuator implemented on our platform).

Reflecting the morphology of DynoClimber, the leg-coordination model consists of two identical motors with shaft angles $\Theta = (\theta_1, \theta_2) \in \mathbb{T}^2$, each subject to the traditional second-order linear motor model:

$$\frac{\ddot{\theta}_i JR}{k_\tau} + \frac{\dot{\theta}_i}{k_v} = V, \quad (21)$$

where θ is output shaft angle, J is the moment of inertia of the motor, output shaft and mechanism, R is the winding resistance of the motor, k_τ is the torque constant of the motor, k_v is the speed constant of the motor, and V is the terminal voltage. This is an equivalent model to that employed by Poulakakis et al. (2004), with the caveat that we base our

analysis on a system which supplies voltage, not current, to the motors.

It is important to note here that variable loading and frictional effects from the dynamics of climbing (manifested as substantial time variations in J and k_v) dominate the behavior of the system, and any forces applied to the foot are reflected through a highly backdriveable mechanism as torques applied to the motor.

We thus wish to minimize our dependence on an accurate system model as the parameters of this model could vary widely based on the operating regime of the robot, and therefore generalize the motor model from (21) to include all constant inertia, Rayleigh-damped, Hooke's law spring potential mechanical systems of the form

$$k_2\ddot{\theta} + k_1\dot{\theta} = V \tag{22}$$

where $k_1, k_2 > 0$. We construct a controller which will achieve its goals regardless of the choice of k_1 and k_2.

We represent the 'robot' with two identical but independent actuator models, each standing in for one of the robot's motors and linkages:

$$k_2\ddot{\Theta} + k_1\dot{\Theta} = \begin{bmatrix} V_1(\Theta) \\ V_2(\Theta) \end{bmatrix}. \tag{23}$$

The controller is designed to dynamically 'couple' these putatively independent motors through a memoryless nonlinear output feedback law that respects their terminal voltage magnitude constraints and guarantees that in the absence of external perturbations they will converge as a coupled system to the desired limit cycle on the torus of paired shaft angles and its tangent space of paired velocities from almost every initial condition. In employing this abstraction we explicitly neglect the motors' mechanical coupling through the body, and relegate the actual task-related properties of body state to the role of 'noise' felt as unmodeled 'load' perturbations on independent motor shafts. We turn to the mechanical design of DynoClimber to demonstrate effective climbing as long as its legs are maintained in a roughly antiphase relationship. In further defense of our coarse abstraction we observe that these models are sufficiently complex that so far the only analytical results for work-directed controllers encompassing physical actuator models explicitly coupled to the physical body state model have been obtained for one-degree-of-freedom bodies (e.g. such as that of Kodistchek and Buehler (1991)) and that we see the present analysis as a first step along the way to that more informative but far less tractable problem. We also observe that no smooth work-directed scheme has heretofore been shown to converge even on $\mathbb{T}^2$.

5.3.1. Coordination controller definition Formally, letting $V := (V_1, V_2)$ be the voltage command signal and $\delta := \theta_1 - \theta_2$ we take

$$V(\Theta) = V_{\max}\begin{bmatrix}1\\1\end{bmatrix} - h(\delta)\cdot\begin{bmatrix}\mathrm{u}\circ\sin(-\delta)\\ \mathrm{u}\circ\sin(\delta)\end{bmatrix} \tag{24}$$

where the unit step function, u, outputs the scalar value 1 if its argument is positive and outputs 0 elsewhere, while $h : \mathbb{S}^1 \to \mathbb{R}^1$ is any smooth, even, positive function that vanishes if and only if its argument is 0 or π.

Combining controller and plant, our system is

$$k_2\ddot{\Theta} + k_1\dot{\Theta} = V_{\max}\begin{bmatrix}1\\1\end{bmatrix} - h(\delta)\cdot\begin{bmatrix}\mathrm{u}\circ\sin(-\delta)\\ \mathrm{u}\circ\sin(\delta)\end{bmatrix}. \tag{25}$$

To verify that our control input is smooth, we show that our term containing step functions,

$$v(\delta) = h(\delta)\cdot\begin{bmatrix}\mathrm{u}\circ\sin(-\delta)\\ \mathrm{u}\circ\sin(\delta)\end{bmatrix}$$

is differentiable. First, for $\delta \in (0, \pi)$), noting that $\mathrm{u}\circ\sin(\delta) = 1$ and $\mathrm{u}\circ\sin(-\delta) = 0$,

$$\frac{dv}{d\delta}\,|_{\delta\in(0,\pi)} = dh/d\delta\cdot\begin{bmatrix}0\\1\end{bmatrix}$$

and for $\delta \in (-\pi, 0)$, similarly,

$$\frac{dv}{d\delta}\,|_{\delta\in(-\pi,0)} = dh/d\delta\cdot\begin{bmatrix}1\\0\end{bmatrix}.$$

Because h is non-negative and smooth with isolated zeros when its argument is 0 or π, $v(0) = v(\pi) = 0$, and $dh/d\delta \to 0$ as $\delta \to 0$ or π from either side. Since the derivative of a step function is undefined at 0, we define $(dv/d\delta)(0) = (dv/d\delta)(\pi) = 0$. This makes $dv/d\delta$ continuous everywhere and demonstrates that our control input is smooth despite the presence of step functions.

We make a final informal observation about our controller: since the controller specifies motor voltages directly, it keeps at least one motor operating along its speed-torque curve at all times. Our present implementation provides no guarantee that motor current will not fall below the motors' sustainable current ratings; using this control framework to specify voltages, as we have done here, can indeed require the motors to overheat. DynoClimber has not exhibited thermal problems, a trait we discuss in Section 6.1.1.

5.3.2. Proof of correctness For $\alpha \in \mathbb{S}^1$ denote the α-translate of the diagonal in $\mathbb{T}^2$ as

$$\Delta_\alpha := \{(\theta, \theta+\alpha) \mid \theta \in \mathbb{S}^1\}.$$

Proposition 1. *The anti-diagonal tangent space,*

$$T\Delta_\pi := \{(\theta_1, \theta_2, \dot{\theta}_1, \dot{\theta}_2) \,|\, \theta_1 = \theta_2 + \pi, \dot{\theta}_1 = \dot{\theta}_2\} \tag{26}$$

is an attracting invariant set whose domain includes $T(\mathbb{T}^2) - T\Delta_0$.

Proof. Rewrite (25) in the new coordinates,

$$\begin{bmatrix}\rho_1\\ \rho_2\end{bmatrix} = \begin{bmatrix}\theta_1 - \theta_2\\ \theta_1 + \theta_2\end{bmatrix} \tag{27}$$

yielding

$$\begin{bmatrix} V_1(\Theta) \\ V_2(\Theta) \end{bmatrix} = \begin{bmatrix} \frac{\ddot{\rho}_1+\ddot{\rho}_2}{2} \\ \frac{\ddot{\rho}_2-\ddot{\rho}_1}{2} \end{bmatrix} k_2 + \begin{bmatrix} \frac{\dot{\rho}_1+\dot{\rho}_2}{2} \\ \frac{\dot{\rho}_2-\dot{\rho}_1}{2} \end{bmatrix} k_1 \ .$$

Solving for $\ddot{\rho}_2$ in the second equation, substituting it into the first, and simplifying yields

$$\begin{aligned} \ddot{\rho}_1 k_2 + \dot{\rho}_1 k_1 = &- h(\rho_1) \cdot \mathrm{u} \circ sin(-\rho_1) \\ &+ h(\rho_1) \cdot \mathrm{u} \circ sin(\rho_1) \qquad (28) \\ \ddot{\rho}_2 k_2 + \dot{\rho}_2 k_1 = &V_1(\Theta) + V_2(\Theta) . \qquad (29) \end{aligned}$$

Noting that ρ_1 is decoupled from ρ_2, we introduce a LaSalle function over $T\mathbb{S}^1$,

$$\begin{aligned} E(\rho_1, \dot{\rho}_1) &= k_2 \cdot \frac{\dot{\rho}_1^2}{2} - H(\rho_1) ; \\ H(\rho_1) &:= \int_0^{|\rho_1|} h(x)\, dx. \qquad (30) \end{aligned}$$

Here $h(\rho_1)$ goes to 0 smoothly as $\rho_1 \to 0$, so H is smooth. By construction, $h(x) > 0 \, \forall x \in \mathbb{S}^1 - \{0, \pi\}$, and $h(0) = h(\pi) = 0$. $H(\rho_1)$ is strictly decreasing in $|\rho_1|$, and therefore takes its minimum at π and its maximum at 0, with no other critical point. It follows that $(\pi, 0)$ is the unique minimum of H.

Taking the time derivative of E along the motions of the system, and recalling that $h(\cdot)$ is an even function, we find

$$\begin{aligned} &\dot{E}(\rho_1, \dot{\rho}_1) = \\ &\quad k_2 \dot{\rho}_1 \ddot{\rho}_1 + h(\rho_1)\, \dot{\rho}_1 (\mathrm{u} \circ \sin(-\rho_1) - \mathrm{u} \circ \sin(\rho_1)) . \end{aligned} \qquad (31)$$

After substituting $\ddot{\rho}_1$ from (28) and cancelling terms, we obtain

$$\dot{E}(\rho_1, \dot{\rho}_1) = -k_1 \dot{\rho}_1^2. \qquad (32)$$

Thus, $\dot{E}$ is negative semi-definite and E is a suitable LaSalle function.

Examining the inverse image,

$$\dot{E}^{-1}(0) = \{(\rho_1, 0) \,|\, \rho_1 \in \mathbb{S}^1\} \qquad (33)$$

we find the only invariant subsets of $\dot{E}^{-1}(0)$ occur at the zero section corresponding to the critical points of H, i.e. when $\dot{\rho}_1 = 0$ and $h(\rho_1) = 0$, which implies that $\rho_1 = 0$ or $\rho_1 = \pi$. Since $(\pi, 0)$ is a minimum of E, while $(0, 0)$ maximizes E in ρ_1, the former is an attractor and the latter a repellor, and the result follows.

□

Corollary 1. *The restriction dynamics on the attracting invariant submanifold $T\Delta_\pi \approx T\mathbb{S}^1$ gives rise to an almost globally asymptotically stable limit cycle.*

Proof. On $T\Delta_\pi$ we have $(\rho_1, \dot{\rho}_1) = (\pi, 0)$, hence, the restriction dynamics are given by $\ddot{\rho}_2 k_2 + \dot{\rho}_2 k_1 = 2V_{\max}$, and the system yields a single attracting limit cycle of the form

$$(\rho_2, \dot{\rho}_2)(t) = (\rho_2(0) + \omega t, \omega), \qquad (34)$$

where $\omega := 2V_{\max}/k_1$. □

6. Robot design and physical implementation

In order to investigate the effectiveness and applicability of the models of dynamic climbing presented thus far, and to test the efficacy of the proposed climbing template as a means to anchor a physical robot subject to realistically available power density at a utilitarian scale, we have built a series of mechanical prototypes. These bipedal robots represent our initial efforts to synthesize a robotic platform that effectively exploits its dynamics to achieve effective vertical running.

To maintain a focus on the template dynamics, we sought to decouple the vertical and lateral climbing motions from other key environmental interactions required for climbing, such as adhesion to the wall and roll dynamics. We chose to work with claw-like feet on a carpet substrate, a combination that proved effective as a starting point for RiSE v1.0 (Autumn et al. 2005), and on which that robot's fastest climbs have been recorded (Haynes and Rizzi 2006). This initial setting gives us confidence that the attachment developments that have enabled RiSE to move from carpet to brick, stucco, concrete, etc. (Spenko et al. 2006, 2008) may be adaptable to our dynamic climber as well. It also provides for an equitable comparison of the robots' relative performances.

6.1. Mechanical structure and design

The basic mechanical design is adapted directly from the two-dimensional simulation described in Section 4, which is composed of a rigid body and two linearly moving arms with springs. The resulting robot, depicted in Figure 9, features two motors, each driving a crank–slider mechanism attached to an arm. As in simulation, each leg has an energy-storage spring in parallel with the crank–slider. Each foot also features a pair of passive-wrist springs which act in series with the drive mechanism. These passively connect the claw to the arm and are extended during the beginning of the stance phase, acting to mitigate the loading forces on the robot. Heavy components, such as the motors and electronics, are located below the cranks in order to position the COM lower in correspondence to the idealized mass distribution of the template. The frame of the robot was initially constructed from ABS plastic, and later from machined aluminum. The transmission system is composed of a bevel gear pair, a pulley pair, sliders (steel shafts and linear bearings), and aluminum links. The sprawl angles of both arms are adjustable with several pre-settings, including the setting of 10°, which corresponds to the effective sprawl angle used by geckos and cockroaches. The robot's physical parameters are summarized in Table 2.

To minimize out-of-plane rolling, we outfitted the robot with a roll-stabilization bar, as seen in Figure 9. This bar extends laterally 20 cm on both sides and approximates the function of multiple legs in reducing roll dynamics. The template only considers motions in the climber's frontal plane; the roll-stabilization bar is implemented in

Table 2. Physical parameters common to both initial and modified robot versions.

Body size	400 mm × 116 mm × 70 mm (excluding cables)
Wrist spring stiffness	640 N/m
Parallel spring stiffness	58 N/m
Motor	Maxon RE 25 118752
Gear head	Maxon Planetary Gearhead GP 32A 114473 33:1 Gear ratio
Encoder	Maxon digital encoder HEDS55 110515 500 count/turn
Leg sprawl angle	10° from centerline

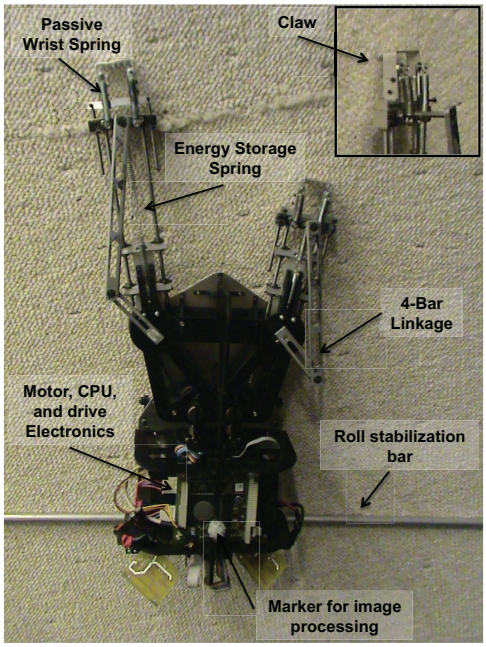

Fig. 9. An annotated picture of the modified DynoClimber hanging on the climbing track.

an attempt to enforce that assumption. In future work, this bar could be replaced by active rear legs designed to apply forces normal to the wall which counteract the robot's natural rolling dynamics.

We chose to implement a passive attachment strategy where the claw is rigidly attached to the hand. The bent teeth of the claw, shown in Figure 9, provide a simple mechanical implementation of directional attachment, in that they engage the substrate when the leg is being pulled down, and release when pushed up. A slight pitch angle introduced by a block under the rear of the robot ensures that the extended foot is closer to the wall than the retracted foot and aids in attachment at the expense of a slightly reduced effective stride length. While simple and generally effective, the fully passive nature of this attachment mechanism does, on occasion, result in lost footholds. Future foot designs will include an actuator at the hand which will improve the reliability of attachment, and provide for control of the phasing of attachment and detachment.

The resulting robot was, due to alterations to the electronics which increased their mass and changes in the design to increase the structure's rigidity and strength, 20% heavier than projected. This initial climber, despite achieving record climbing speed at the time, had a number of mechanical and electrical flaws. Its ABS plastic baseplate flexed enough to allow occasional drive belt slippage, and the motor driver filtering circuitry did not have a sufficiently low break frequency, allowing too much ripple with a supply of more than 18 V. Owing to concerns about the weight of the robot, structural strength of the body, and the limits of the early version of the power electronics, the robot was initially designed to climb at a reduced speed. This speed reduction was implemented via a gear reduction of the motor of 66:1 rather than the 50:1 ratio originally determined to be optimal through simulation. After testing, however, it became clear that the robot's locomotion would be substantially more dynamic if its gear ratio were reduced. Even with these limitations, and without the benefit of the self-excited, work-directed controller, the robot (as shown below in Section 6.3) was able to climb at high speeds and in a manner predicted by our design simulations.

In order to overcome the shortcomings of the initial version of the hardware a modified version of the robot featuring a more robust mechanical structure and an updated electronics infrastructure capable of operating in the > 24 V range was built. The alterations included an all new aluminum frame and new motor drive electronics. These modifications, however, added an additional 200 g to the robot, resulting in a new total mass of 2.6 kg. In light of these changes to the robot it was calculated that a new gear reduction would be necessary to optimize the robot's climbing speed. Simulation studies indicated that a total gear reduction of 56:1, which is closer to the original design specification, would maximize climbing speed. Prospective changes were prototyped in the design model by a literal transcription of parameters, although due to the speed limitations of the simulation engine, the design model could not be tested for a comprehensive set of parameter variations. Instead, the vertical power stroke model (Section 5.1) was simulated over large gear ratio (altering F_s and l_s reciprocally in the model) and stride-length ranges (direct changes to l_s) to determine roughly optimal gear ratio choices. Two criteria were used to determine optimality:

the design choices needed to optimize climbing speed while ensuring that steady-state climbing occurred with the motors drawing less than their continuous current ratings.[13]

6.1.1. Comparison of power stroke model and robot In Table 3, we give the parameters used in both versions of the physical robot (see Section 6.1 for a more complete description) and the best physical equivalences for the vertical power stroke model. Table 5 verifies that both parameter sets meet the criteria of our proof of stability.

6.2. Experimental setup and procedure

To evaluate the robot climbing performance, a 4 m × 0.8 m carpet-surface vertical climbing wall was built, part of which is shown in Figure 9. A commercial six-axis force sensor (AMTI HE6x6) was built into a panel of the wall to collect interacting forces between the left foot of the robot and the wall. A vision system composed of a commercial HD video camera (SONY HDR-SR1) and two spotlights for robot motion tracking is located 4 m away facing the climbing wall. In order to simplify the off-line analysis of the visual data, the robot is painted black and two markers are installed rigidly on the body for size calibration.

Both force data and video data are collected while the robot climbs. Video streams are exported into sequential images for post-processing in Matlab. Each color image is converted into black and white by setting threshold empirically and the 'white' objects in the image are distinguished from each other by a labeling function and by their geometric relations. For each run the robot was started from rest at the bottom of the track and the last 5 seconds of climbing were analyzed. In this section we describe experimental results from two versions of the robot. Videos of the robots climbing can be seen in Extension 1 and Extension 2.

6.3. Initial (2.4 kg) robot performance

Figure 10 shows the trajectory and velocity of the center of mass of the initial 2.4 kg robot while climbing. This figure shows the final 16 steps (8 per leg) after the robot had accelerated from rest to a steady-state climbing speed. Subplots (A) and (C) show the vertical velocity oscillates substantially during each stride, but averages to about 30 cm/s as the robot climbs with a stride frequency of 1.8 Hz. Figure 11 compares the ground reaction forces and velocities of the robot and a simulation of a similar 2.4 kg version that has been modified to match the larger gear reduction and lower applied voltage used in the experiments shown in Figure 10.

The lateral position and velocity, shown in Figure 10, subplots (B) and (D) indicate that the lateral oscillations are larger than the animal-inspired template, with lateral velocities about 1.5 times as large as the scaled template. As predicted by simulation, the lower stride frequency results in larger lateral swings with each stride. The pendular

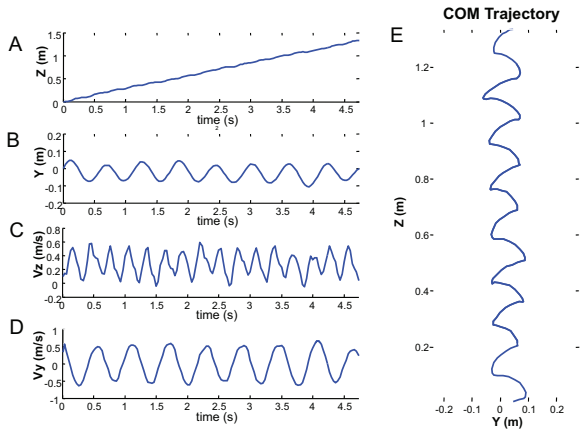

Fig. 10. Video-based marker data for eight strides of the initial 2.4 kg robot climbing: (A) vertical displacement, (B) lateral displacement, (C) vertical velocity, (D) lateral velocity, and (E) the path of the center of mass during climbing.

frequency of the original template body is generally slower than the template's stride frequency. However, as stride frequencies are reduced, and therefore near the pendular frequency, the rotational motion of the climber becomes dramatically more pronounced. The COM position plot (E), shows how at the end of each stride the motion of the robot is largely lateral. With each new foot placement the robot begins to reverse direction and accelerate upwards again.

The top row of Figure 11 shows the lateral and horizontal ground reaction forces for both the 2.4 kg simulation and the left foot of the 2.4 kg robot. Owing to the location of the force plate on the climbing wall, only force data for the left foot is available. The robot's legs remain attached for slightly longer each stride than predicted by simulation due to the existence of a double support phase: using the passive attachment mechanism, a foot is disengaged from the substrate after the other foot has engaged and begun pulling up the robot. Consequently, slightly larger magnitude attachment forces and foot-attachment duty factors of about 60% are seen on the robot.

The second and third rows show, for a single stride, the traces of the vertical and lateral speed, which are very close in both magnitude and phasing. The experimental velocity data's coarseness stems from the limited frame rate of the camera used to record the motion. While the simulation climbs slightly faster than the robot it does not incorporate artifacts associated with attaching and detaching from a compliant substrate or friction of the body against that substrate.

These initial results demonstrate that fast, dynamically stable vertical running with a template-inspired bipedal climbing robot is achievable. Furthermore, an examination of the stride dynamics indicates that the robot successfully recreates the lateral motions and ground reaction force patterns seen in the template and in the animals. The self-stabilizing nature of the resulting gait is highlighted in the

Table 3. Vertical power stroke model and robot parameters.

Parameter	Description	Units	Initial robot	Modified robot	Initial power stroke	Modified power stroke
M	Body mass	kg	2.4	2.6	2.4	2.6
l_s	Stroke length	m	0.12	0.13	0.12	0.13
V	Battery Voltage	V	18	30	18	30
r	Pinion gear radius	m	N/A	N/A	0.0382	0.0414
l_c	Crank length	m	0.6	0.65	N/A	N/A
G	Gear ratio	·	66 : 1	56.6 : 1	66 : 1	56.6 : 1
k	Energy storage spring	N/m	58	58	58	58
F_s	Output stall force	N	Varies	Varies	403	531
τ_s	Motor stall torque	Nm	0.233	0.388	0.233	0.388
v_{nl}	Output no-load speed	m/s	Varies	Varies	0.62	1.30
ω_{nl}	Motor no-load speed	rad/s	1,068	1,780	1,068	1,780
F_c	Output continuous force	N	Varies	Varies	41.5	32.81
τ_c	Motor continuous torque	Nm	0.0240	0.0240	0.0240	0.0240
	Controller	·	Mirror law (19)	SEWD (20)	Constant voltage	Constant voltage

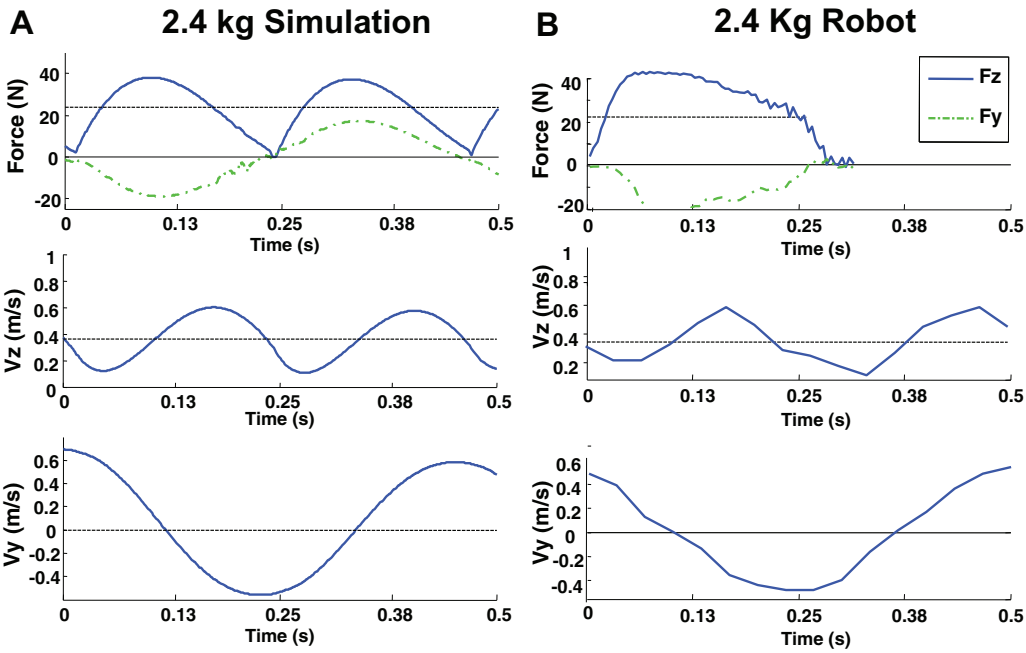

Fig. 11. Ground reaction forces and vertical (Vz) and horizontal (Vy) center of mass velocities for the 2.4 kg simulation and robot. Note: due to the location of the force plate, only forces for the left foot of the robot were measured.

first video attachment where the robot is shown quickly recovering from a missed foothold near the top of its climb.

Past tradition in the locomotion literature has been to provide qualitative comparison of animal, simulation, and robot test trajectories as we do here in assessing the quality of model fit (Altendorfer et al. 2001; Autumn et al. 2006). Newer statistical methods of phase comparison (Revzen and Guckenheimer 2008) suggest a much more intensive data set than presently available in our prototype implementation can deliver a far more precise estimate of fit, but such a statistical comparison lies beyond the scope of the present paper. The comparison of the robot's motion with the simulation also demonstrates good correspondence, with the average upward velocity, peak lateral velocities, and peak ground reaction forces agreeing to within about 10%. In addition, the phasing between lateral and vertical motions and the ratios of the lateral and vertical forces are all preserved.

6.4. *Modified (2.6 kg) robot performance*

As described in Section 6.1, the electrical and mechanical limitations in the original design induced the design and construction of a modified version of the robot of mass

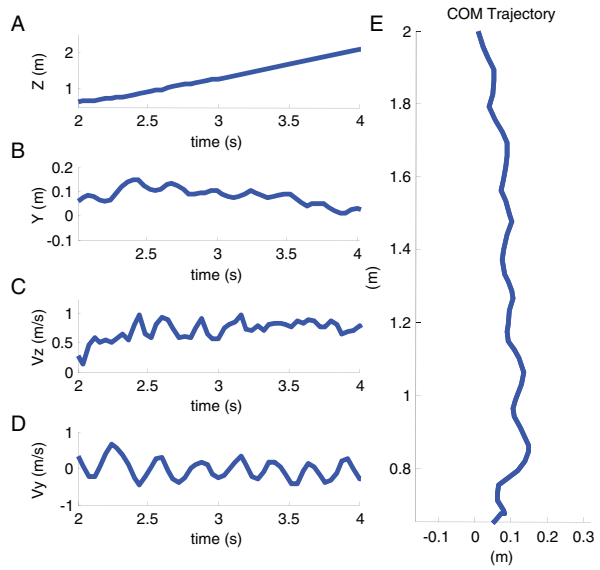

Fig. 12. Video-based marker data for 2 seconds of the modified 2.6 kg robot climbing with a 32 V supply: (A) vertical displacement, (B) lateral displacement, (C) vertical velocity, (D) lateral velocity, and (E) the path of the center of mass during climbing.

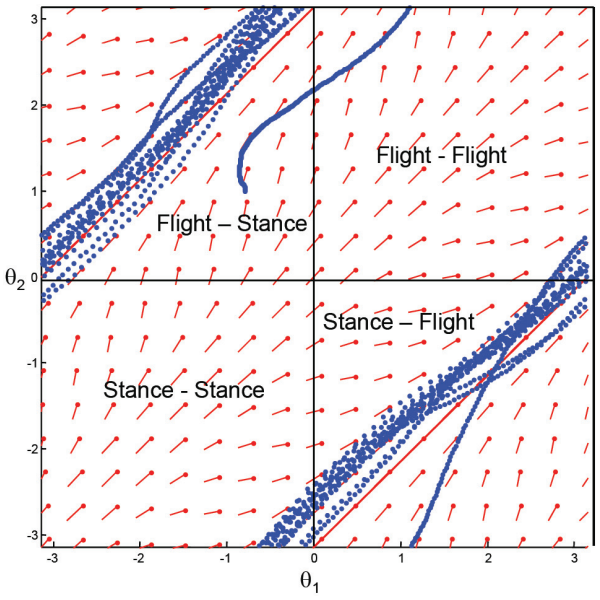

Fig. 13. Robot motor state overlaid on top of the phase portrait of the controller vector field. The robot encoder data points are superimposed on the controller vector field and show convergence to the desired 180° out-of-phase behavior.

2.6 kg. The results of running the robot with these design changes and the self-excited, work-directed control strategy (see Section 5.2.2) are shown in Figure 12.

In order to test the performance capabilities of the robot, it was run with an input voltage set to both 20 V and 32 V. We found that the average speed of climbing for a 20 V input was 38.8 ± 2.8 cm/s. These runs with an input voltage comparable to that used on the initial robot show the inclusion of the self-exciting, work-directed controller, resulted in an increased climbing speed of about 20%. With a 32 V supply the robot ran at a record breaking 67 cm/s, which in both an absolute and in a scale-independent sense is faster than the cockroach climbing that inspired the dynamic climbing template. Climbing at this speed is shown in the second video attachment.

Figure 12 shows the COM trajectory and velocity profiles for a sample run at 32 V. While there are distinct differences between these results and those with the initial prototype shown in Figure 10, the characteristic oscillations in lateral position and velocity, shown in subplots (B) and (D), respectively, are still present. Furthermore, subplot (E) shows that the magnitude of the lateral oscillations has decreased from the initial prototype results and corresponds better to high-speed oscillations observed in the template and animals. The periodic variation in vertical position and velocity, in subplots (A) and (C), respectively, is less prominent, though there are still variations that indicate this oscillation is likely still present but significantly more noisy. Examination of the velocity profile shows that as steady-state climbing is achieved, the robot scales the wall at an average vertical velocity of 67 cm/s, which as previously mentioned makes DynoClimber the fastest vertical climbing robot to date.

Along with comparing the characteristic motion patterns of the template and experimental platform, the efficacy of the leg coordination control was also examined. Figure 13 shows the angular position of the two motors throughout a 32 V trial and is overlaid on the vector field used to dictate desired motor position. These results show that the leg coordination controller quickly forces the legs into a 180° phase offset and maintains that offset during the entire run.

In the short term, electronic infrastructure provides the practical limit on the maximum voltage that can be applied. Note that electromagnetic motors are only thermally affected by motor current; voltages larger than nominal are still ‘safe’ as long as motor current is kept to permissible values and the motor does not spin faster than its specified peak operational speed. As voltage is increased, additional care must be taken to ensure these criteria are met. The robot’s legs must be loaded carefully, with neither too much nor too little resistance. Running the robot’s legs at a high voltage with a heavy load is likely to cause the motors to draw excessive current and overheat, while spinning the motors unloaded could permit them to exceed the motor’s maximum permissible speed. However, for a range of acceptable motor speeds, this increase in voltage enables an impressive increase in power output.

The ability to sustain climbing at these velocities and voltage levels for extended periods is uncertain, but the need for high-speed vertical climbing is typically intermittent. For example, even if due to motor thermal constraints this speed could only be maintained for 1 minute, the robot would still be able to scale a height of 40 m before stopping.

6.5. Discussion of results

With our spring-assisted dynamic climbing robot, DynoClimber, we have developed and implemented an operational platform design that exploits bioinspired COM motions and ground reaction forces to produce vertical climbing speeds of over one and a half body-lengths per second. The robot performance matches the predictions of the dynamic simulation and analytical models quite well respecting climbing speed, ground reaction force profiles, and velocity phasing. See Table 4 for a comparison of robot and model, as well as scaled animal, climbing speeds. This agreement suggests that the argument in Section 4.4 is correct in predicting that we are near the largest and fastest climber that can implement template-based climbing dynamics with the currently employed off-the-shelf motors.

When compared with both the detailed design-oriented simulation described in Section 4 and the simple power-stroke model introduced in Section 5.1, the physical platform climbs roughly 30% slower than predicted. This result is unsurprising given the frictionless environment and perfect attachment of the simulation models. However, the models' abilities to anticipate rough performance trends is well brought out in Table 4: both come close to predicting the 223% empirical increase in steady-state climbing speed from the initial (2.4 kg) design to the modified (2.6 kg) case (the design simulation predicts a 220% increase while the vertical power stroke model predicts a 227% increase).

To determine the 'scaled roach' vertical speed values, we applied the scaling laws derived in Section 3 to the measured cockroach mass and speed from Goldman et al. (2006). Moreover, while the robot and both simulations indicate that our initial climber would be incapable of achieving scaled-template-like vertical speeds, the modified climber is able to do so in both simulation and the physical world.

In general, we find the rough agreement between the detailed simulation and the vertical power stroke models particularly notable: despite the design model's relative complexity (rotational dynamics, crank–slider transmission, wrist springs, and rigid body dynamics), the greatly simplified purely vertical power stroke model climbs within 10% of the simulation's speed. It is also notable that the correspondence of this simple model applies to both the initial and modified robot cases. The small discrepancy between these vastly differently abstracted models suggests the extent to which a climber's power train determines its vertical velocity.

This agreement reinforces our use of simplified models to make first-order design decisions. While a detailed simulation is required to support crucial decisions bearing on implementation details (changing the robot's mass distribution, for instance), overarching questions concerning the soundness of the power stroke concept and its impact on vertical climbing behavior can be explored far more thoroughly (and, indeed, with some consequent mathematical guarantees) using the vertical power stroke model. Thus, the introduction of this coarse, reduced-order model allows us simulate power train design choices (i.e. motor choice, gear ratio, or stride length) much more extensively than would be possible with the high-fidelity simulation alone. Moreover, provided that the unmodeled dynamics are stable and not disruptive, that model delivers equivalent results.

7. Conclusion and future work

Biologists' discovery of a template, a common dynamical pattern, for climbing in diverse animal species (Goldman et al. 2006) inspired our adaptation of their simulation model, resulting in a physically instantiated, bipedal, dynamical vertical climber. Systematic scaling arguments along with numerical and mathematical modeling result in design specifications for a robot that exhibits a strong correspondence to the original template model despite accommodations to the exigencies of commercially available actuators. The addition of a force-assist spring in parallel with the actuator in the legs and the switch to a force controlled actuation scheme allow conventionally actuated legged robotic climbing at animal-like speeds, even approaching the upper limits of commercially available power densities. In addition, it appears that the characteristic force and motion patterns of the animals and the steady gaits exhibited by the template are reproducible in the physically anchored version, the robot.

In addition to this constructive demonstration that the Full–Goldman template (Goldman et al. 2006) dynamics can be successfully anchored in a synthetic dynamic climber, this paper has presented an analysis of the internal vertical dynamics of the power-stroke system and shown that it is inherently stable. This, coupled with the development and proof of stability of the gait coordination controller, has laid an analytical foundation for the study of vertical dynamical climbing.

Future theoretical work, however, will be required to fully understand how the robot's physical structure and control scheme interact to determine its lateral stability. This design study motivates more practical empirical work investigating the effect of increased climbing speed on the attachment and detachment of feet capable of adhering to smooth surfaces. In addition to enabling higher speeds, proper exploitation of the locomotion dynamics could also lead to greater maneuverability without having to increase the kinematic complexity of the design. Eventually, however, the body dynamics that result in fast, stable climbing will be integrated into robots with more limbs to achieve a truly utilitarian dynamical robot that can operate on a number of surfaces and on substrates with varied geometries.

Accumulating simulation results (Goldman et al. 2006; Lynch et al. 2011b) support the hypothesis that lateral and rotational stability for climbers is improved by generation of large lateral inpulling forces. Such simulation studies suggest that sprawled posture may also have some energetic benefit for a DC-servo-driven climber albeit likely not for

Table 4. Climber and model performance.

Platform	Initial climber	Modified climber
Design simulation (Section 4)	0.44 m/s	0.85 m/s
Power stroke model: $\bar{\zeta}^*$ (18)	0.41 m/s	0.93 m/s
Physical robots	0.30 m/s	0.67 m/s
Scaled roach (Goldman et al. 2006)	0.61 m/s	0.62 m/s

a biologically muscle-driven climber (Lynch et al. 2011b). More recent analysis and simulation suggests that the bifurcation to instability as the sprawl angle is reduced should be commonly observable, not simply across scale, but across driving frequency as well (Lynch et al. 2011a). Testing this hypothesis in a physical platform entails studying DynoClimber's response to controlled perturbations for different sprawl angles. Our hypothesis suggests that for some sprawl angle larger than zero, the robot's settling time following perturbations should be minimized.

In addition to future experimental work to examine the effect of leg sprawl angle on vertical climbing, this platform could be used to investigate why animals alter their horizontal force generation patterns as the inclination of the substrate changes from horizontal to vertical.

In conclusion, we have built the first dynamical vertical climbing robot. The successful scaling and implementation of the bio-inspired template has enabled us to explore the possible advantages of this novel design that uses passive–dynamic elements. Because the robot exhibits a scaled version of the dynamics measured in diverse animal species, we are also hopeful that it might be useful as a physical model to generate a next round of testable hypotheses that might lead to new discoveries in animal climbing.

Notes

1. See http://berkeley.edu/news/media/releases/2002/09/rfull/robots.html
2. Mounting evidence (Goldman et al. 2006) suggests that animals switch from outward to inward lateral force generation when they transition from horizontal to vertical running.
3. The template does not brachiate or actively swing in a pendulous manner to raise its center of mass. Rather, sprawl angle, when teamed with an adequately rapid stride frequency, minimizes angular deviation as evidenced by the minimal angular excursion demonstrated by the template.
4. The parameters used to generate Figure 2(C) were body mass = 2 g, body dimensions = 4 cm $\times$ 0.95 cm, $l_1 =$ 0.71 cm, $l_2 = 0.84$ cm, $\beta = 10^\circ$, $L_0 = 1.54$ cm, $z =$ 0.6, $k = 6\text{N} \cdot \text{m}^{-1}$, $\gamma = 0.09\text{N} \cdot \text{s} \cdot \text{m}^{-1}$, $f = 9$ Hz. The attachment duty factor in the model is 0.46. The rigid body has a moment of inertia of $8 \times 10^{-7}\text{kg} \cdot \text{m}^2$, on the same order of magnitude of as cockroaches ($2 \times 10^{-7}\text{kg} \cdot \text{m}^2$) (Schmitt et al. 2002).
5. DynoClimber's morphology as depicted in Figure 9 bears significant kinematic resemblance to the template of Figure 1. Anchoring that template in a robot with more legs is certainly possible, since the model was constructed to help understand the locomotion strategies of four- and six-legged animals. The specific morphology and controller for such a robot would apply a resultant force to the robot that matched the force applied to the template.
6. Although the Froude and Strouhal numbers are invariant to scale, the specific values depends upon the characteristic length l_C of the template. For upright runners, the 'leg length' is typically used, which is the distance from the hip to the foot. However, it is not clear whether this convention applies to sprawled posture runners. For example, in our climber, if the stroke length of the prismatic actuator is used as the characteristic length, the template and scaled climber have a Froude number of 0.73; if the leg length, as defined above, is utilized, the Froude number is 0.45; and if the body height, the distance from the extended foot to the tail, is used, it drops to 0.28. While this discrepancy may complicate cross-platform comparisons, the non-dimensional parameters remain invariant to scale regardless of the characteristic length chosen as long as the dynamic similarity laws are observed.
7. Body-lengths per second scales as $\alpha_V/\alpha_L = \alpha_L^{-\frac{1}{2}}$.
8. We choose to use rotational motors due to their high power density and extensive selection readily available from manufacturers such as Maxon, see http://www.maxonmotorusa.com.
9. Moreover, De et al. (2011) demonstrates that motors operating continuously produce less thermal energy whilst performing a given amount of mechanical work than those operating intermittently.
10. In contrast, as for all multi-jointed locomotion models Raibert (1986); Kodistchek and Buehler (1991); Ghigliazza et al. (2005), the complete template (Figure 1) entails non-integrable dynamics, whose mathematical analysis will likely require as similarly long a string of focused papers as occasioned by level ground running (Raibert 1986; Kodistchek and Buehler 1991; Ghigliazza et al. 2005; Holmes et al. 2006).
11. See http://www.maxonmotorusa.com.
12. Most attachment failures are caused by inadequate roll stabilization: the robot occasionally rolls in such a way as to lift its flight leg slightly from the wall. If that lift

coincides with the beginning of a leg's stance phase, the passive attachment mechanism permits no recourse and the foot is unable to find purchase.

13. Exact design choices are often determined by readily available part sizes; the gear ratio modification from the initial to the modified version of DynoClimber was physically implemented by changing the belt gear ratio from 1:1 to 12:14, for instance.

Funding

This work was supported in part by DARPA/SPAWAR (contract number N66001-05-C-8025) and by NSF (grant number FIBR EF-0425878). Jonathan Clark was supported by the IC Postdoctoral Fellow Program (grant number HM158204-1-2030).

Acknowledgments

We thank Bob Full and Dan Goldman for numerous discussions and insight related to the scaling and adaptation of their vertical climbing template model. We thank Haldun Komsuoglu for porting his EduBot electronics and controls hardware and software infrastructure to this platform. In addition, we would like to thank Al Rizzi, Martin Buehler, and Aaron Saunders for a number of discussions bearing on design and control of the physical platform, and the anonymous reviewers for their insights and suggestions regarding the organization of the paper. Some of the component pieces of the present account have been offered in preliminary form in various conferences: Clark and Koditschek (2006) (initial actuation analysis); Clark et al. (2006) (initial platform design); Clark et al. (2007) (initial empirical climbing results); and Lynch et al. (2009) (robot controller design).

References

Alexander RM and Jayes AS (1983) A dynamic similarity hypothesis for the gaits of quadrupedal mammals. *Journal of Zoology* 201: 135–152.

Altendorfer R, Moore N, Komsuoglu H, Buehler M, Brown HBJ, McMordie D, et al. (2001) Rhex: A biologically inspired hexapod runner. *Autonomous Robots* 11: 207–213.

Asbeck A, Kim S, Cutkosky M, Provancher W and Lanzetta M (2006) Scaling hard vertical surfaces with compliant microspine arrays. *The International Journal of Robotics Research* 25: 1165.

Autumn K, Buehler M, Cutkosky MR, Fearing R, Full R, Goldman D, et al. (2005) Robotics in scansorial environments. In Gerhart DWGGR and Shoemaker CM (eds), *Unmanned Systems Technology VII* (*Proceedings of SPIE*, vol. 5804). SPIE, pp. 291–302.

Autumn K, Hsieh ST, Dudek DM, Chen J, Chitaphan C and Full RJ (2006) Dynamics of geckos running vertically. *Journal of Experimental Biology* 209: 260–270.

Balaguer C, Gimenez A, Pastor J, Padron V and Abderrahim C (2000) A climbing autonomous robot for inspection applications in 3D complex environments. *Robotica* 18: 287–297.

Bekey GA (2005) *Autonomous Robots: From Biological Inspiration to Implementation and Control*. Cambridge, MA: MIT Press.

Bevly D, Dubowsky S and Mavroidis C (2000) A simplified Cartesian-computed torque controller for highly geared systems and its application to an experimental climbing robot. *Transactions of the ASME. Journal of Dynamic Systems, Measurement and Control* 122: 27–32.

Birkmeyer P, Peterson K and Fearing R (2009) DASH: A dynamic 16g hexapedal robot. In *IEEE/RSJ International Conference on Intelligent Robots and Systems, 2009 (IROS 2009)*, pp. 2683–2689.

Blickhan R and Full RJ (1993) Similarity in multilegged locomotion: Bounding like a monopod. *Journal of Comparative Physiology* 173: 509–517.

Boggess M, Schroer R, Quinn R and Ritzmann R (2004) Mechanized cockroach footpaths enable cockroach-like mobility. In *Proceedings of IEEE ICRA*, New Orleans, LA, pp. 2871–2876.

Bretl T, Rock S and Latombe JC (2003) Motion planning for a three-limbed climbing robot in vertical natural terrain. In *IEEE International Conference on Robotic and Automotion (ICRA 2003)*, Taipei, Taiwan, vol. 205, pp. 2946–2953.

Buehler M, Koditschek DE and Kindlmann PJ (1990) A simple juggling robot: Theory and experimentation. In *Experimental Robotics I*. Berlin: Springer-Verlag, pp. 35–73.

Buehler M, Koditschek DE and Kindlmann PJ (1994) Planning and control of robotic juggling and catching tasks. *International Journal of Robotics Research* 13: 101–118.

Cavagna GA, Heglund NC and Taylor CR (1977) Mechanical work in terrestrial locomotion: Two basic mechanisms for minimizing energy expenditure. *American Journal of Physiology* 233.

Clark JE, Goldman DG, Lin PC, Lynch G, Chen TS, Komsuoglu H, et al. (2007) Design of bio-inspired dynamical vertical climbing robot. In *Robots: Science and Systems*, Atlanta, GA.

Clark JE, Goldman DI, Chen TS, Full RJ and Koditschek D (2006) Toward a dynamic vertical climbing robot. In *International Conference on Climbing and Walking Robots (CLAWAR)*, vol. 9. Brussels, Belgium: Professional Engineering Publishing.

Clark JE and Koditschek DE (2006) A spring assisted one degree of freedom climbing model. *Fast Motions in Biomechanics and Robotics* (*Lecture Notes on Control and Information Sciences*, vol. 340). Berlin: Springer-Verlag, pp. 43–64.

Daltorio K, Horchler A, Gorb S, Ritzmann R and Quinn R (2005) A small wall-walking robot with compliant, adhesive feet. In *2005 IEEE/RSJ International Conference on Intelligent Robots and Systems (IROS 2005)*. Piscataway, NJ: IEEE, pp. 3648–3653.

De A, Lynch G, Johnson A and Koditschek DE (2011) Motor selection using task specifications and thermal limits. In *TePRA 2011*.

Degani A, Feng S, Brown HB, Lynch KM, Choset H and Mason MT (2011) The Parkourbot - a dynamic bowleg climbing robot. In *Proceedings of the 2011 IEEE International Conference on Robotics and Automations*, Shanghi, China, 9–13 May.

Degani A, Shapiro A, Choset H and Mason MT (2007) A dynamic single actuator vertical climbing robot. In *Proceedings, IEEE/RSH International Conference on Intelligent Robots and Systems*, San Diego, CA.

Full RJ and Koditschek DE (1999) Templates and anchors: Neuromechanical hypotheses of legged locomotion on land. *Journal of Experimental Biology* 202: 3325–3332.

Ghigliazza R, Altendorfer R, Holmes P and Koditschek D (2005) A simply stabilized running model. *SIAM Review* 47: 519–549.

Goldman DI, Chen TS, Dudek DM and Full RJ (2006) Dynamics of rapid vertical climbing in a cockroach reveals a template. *Journal of Experimental Biology* 209: 2990–3000. DOI: 10.1242/jeb.02322.

Gregorio P, Ahmadi M and Buehler M (1997) Design, control, and energetics of an electrically actuated legged robot. *IEEE Transactions on Systems, Man, and Cybernetics, Part B* 27: 626–634.

Guckenheimer J and Holmes P (1983) *Nonlinear Oscillations, Dynamical Systems, and Bifurcations of Vector Fields*. Berlin: Springer.

Haynes G and Rizzi A (2006) Gait regulation and feedback on a robotic climbing hexapod. In *Proceedings of Robotics: Science and Systems*, Philadelphia, PA.

Haynes GC, Khripin A, Lynch G, Aaron Saunders AAR and Koditschek DE (2009) Rapid pole climbing with a quadrupedal robot. In *Proceedings IEEE International Conference on Robotics and Automation*.

Hollerbach JM, Hunter IW and Ballantyne J (1992) A comparative analysis of actuator technologies for robotics. In *The Robotics Review 2*. Cambridge, MA: The MIT Press, pp. 299–342.

Holmes P, Full RJ, Koditschek DE and Guckenheimer J (2006) The dynamics of legged locomotion: Models, analyses, and challenges. *SIAM Review* 48: 207–304.

Kim S, Clark JE and Cutkosky MR (2006) iSprawl: Design and tuning for high-speed autonomous open-loop running. *International Journal of Robotics Research* 25: 903–912.

Kodistchek D and Buehler M (1991) Analysis of a simplified hopping robot. *The International Journal of Robotics Research* 10: 587–605.

Komsuoglu H (2004) *Toward a Formal Framework for Open-loop Stabilization of Rhythmic Tasks*. PhD thesis, University of Michigan.

Kornbluh R, Pelrine R, Eckerle J, Joseph J, Int SRI and Park M (1998) Electrostrictive polymer artificial muscle actuators. In *Proceedings 1998 IEEE International Conference on Robotics and Automation*, vol. 3.

La Rosa G, Messina M, Muscato G and Sinatra R (2002) A low-cost lightweight climbing robot for the inspection of vertical surfaces. *Mechatronics* 12: 71–96.

Lynch G, Clark J and Koditschek D (2009) A self-exciting controller for high-speed vertical running. In *IEEE/RSJ International Conference on Intelligent Robots and Systems, 2009 (IROS 2009)*. Piscataway, NJ: IEEE, pp. 631–638.

Lynch G, Clark JE and Koditschek D (2011a) Stable dynamic vertical climbing - analysis of a reduced order template. *Biological Cybernetics*, in preparation.

Lynch GA, Rome L and Koditschek DE (2011b) Sprawl angle in simplified models of vertical climbing: implications for robots and roaches. In *Proceedings of the 2010 International Conference on Applied Bionics and Biomechanics*, Venice, Italy.

McMahon TA and Cheng GC (1990) Mechanics of running. How does stiffness couple with speed? *Journal of Biomechanics* 23: 65–78.

Murphy MP, Kute C and Sitti M (2011) Waalbot II: Adhesion recovery and improved performance of a climbing robot using fibrillar adhesives. *International Journal of Robotics Research* 30: 118–133.

Murphy MP and Sitti M (2007) Waalbot: An agile small-scale wall-climbing robot utilizing dry elastomer adhesives. *IEEE/ASME Transactions on Mechatronics* 12: 330–338.

Poulakakis I, Smith JA and Buehler M (2004) Experimentally validated bounding models for the Scout II quadrupedal robot. In *Proceedings of ICRA*, pp. 2595–2600.

Provancher WR, Jensen-Sgal SI and Fehlberg MA (2011) ROCR: An energy-efficient dynamic wall-climbing robot. *IEEE/ASME Transactions on Mechatronics* 16(5): 897–906.

Raibert MH (1986) *Legged Robots that Balance* (*MIT Press Series in Artificial Intelligence*). Cambridge, MA: MIT Press.

Revzen S and Guckenheimer JM (2008) Estimating the phase of synchronized oscillators. *Physical Review E* 78: 51907.

Rome LC, Funke RP, Alexander RM, Lutz G, Aldridge H, Scott F, et al. (1988) Why animals have different muscle fibre types. *Nature* 335: 824.

Schmitt J, Garcia M, Razo R, Holmes P and Full R (2002) Dynamics and stability of legged locomotion in the horizontal plane: a test case using insects. *Biological Cybernetics* 86: 343–353.

Schmitt J and Holmes P (2000) Mechanical models for insect locomotion: dynamics and stability in the horizontal plane I. Theory. *Biological Cybernetics* 83: 501–515.

Spenko M, Cutkosky MR, Majidi R, Fearing R, Groff R and Autumn K (2006) Foot design and integration for bioinspired climbing robots. In *Unmanned Systems Technology VIII*. SPIE.

Spenko M, Haynes C, Saunders A, Cutkosky M, Rizzi A, Full R, et al. (2008) Biologically inspired climbiing with a hexapedal robot. *Journal of Field Robotics* 25: 223–242.

Xiao J, Sadegh A, Elliot M, Calle A, Persad A and Chiu HM (2005) Design of mobile robots with wall climbing capability. In *Proceedings of IEEE AIM*, Monterey, CA, 24–28 July, pp. 438–443.

Appendix A: Derivation of the return map

Writing down the closed form of the return map requires us to evaluate the flow of the system at an implicitly defined time. Since the system is affine, its flow can be readily determined from its differential form, first stated in Equation (11):

$$\dot{z} = Az + b.$$

In addition, the initial conditions of the system are defined to be $z_0 =: (0, \zeta)$. Using these initial conditions, the system's flow can be readily written as

$$f^t(z) = e^{At} z_0 - A^{-1} b. \tag{35}$$

The time to flow from $\mathcal{L}_1$ by means of f^t to $\tilde{\mathcal{L}}_1$ is once again a function of the initial condition on the section, $\zeta \in \mathcal{L}_1$:

$$T(\zeta) = min \left\{ t > 0 \mid \ell_1 \circ f^t \ell_2^{\dagger}(\zeta) = l_s \right\}.$$

Constrained operation along the speed–torque curve of the motor force F_m in Equation (10) yields a several-term transcendental appearance of T, resulting in a solution for T which cannot be expressed in closed form and must instead be expressed implicitly by the equation $\ell_1 \circ f^T \ell_2^\dagger(\zeta) = l_s$.

The return map $R(\zeta)$ is then given by

$$\begin{aligned} R(\zeta) &= \ell_2 \circ s \circ f^T \circ \ell_2^\dagger(\zeta) \\ &= \frac{-1}{2\alpha\sqrt{\sigma^2-1}} \\ &\left(e^{\alpha\lambda_2 T}\left[\beta\lambda_1 + \alpha\zeta\right]\cdot\lambda_2 - e^{\alpha\lambda_1 T}\left[\beta\lambda_2 + \alpha\zeta\right]\cdot\lambda_1\right), \end{aligned} \quad (36)$$

with

$$\lambda_1 = -\sigma + \sqrt{\sigma^2-1}, \quad \lambda_2 = -\sigma - \sqrt{\sigma^2-1}$$

defined to be the eigenvalues divided by α.

Differentiating R with respect to ζ and determining $\frac{dT}{d\zeta}$ using the implicit function theorem, we arrive at

$$DR(\zeta) = \frac{\left(2\alpha\zeta\sqrt{\sigma^2-1}\right)e^{\alpha T\left(-\sigma+\sqrt{\sigma^2-1}\right)}}{A_0\, e^{2\alpha T\sqrt{\sigma^2-1}} + A_1}, \quad (37)$$

where

$$A_0 = \left(\beta - \alpha\sigma\zeta + \alpha\zeta\sqrt{\sigma^2-1}\right),$$

$$A_1 = \left(\alpha\sigma\zeta - \beta + \alpha\zeta\sqrt{\sigma^2-1}\right).$$

Appendix B: Proof of stability of the vertical power stroke model

We make several assumptions about system parameters throughout this proof. These algebraic assumptions, listed in Table 5, comprise a sufficient, but not necessary, set of conditions for our stability result, and they are clearly satisfied for any reasonable physical design (including all of our prototypes) as shown in the table.

The third assumption requires a special note. The condition that $\alpha > 0$ is equivalent to $k > 0$: we assume that our climbing model employs an energy storage spring. This assumption is not required for stability, but, rather, is critical to establish the mathematical correspondence to a salient aspect of DynoClimber's power train design as detailed Section 4. (Were $k = 0$, the analysis would be drastically simplified, as the climber's hybrid dynamics would become trivial. The vector field representing climber acceleration on z_1, z_2 would no longer depend on z_1, and the climber would simply converge to that constant velocity at which its motor produced a force of Mg. Thus, while $k = 0$ is a physically valid scenario, it is trivially stable and we do not emphasize its analysis.)

In contrast, β gives the net force on the climber as it begins a stride with no upward velocity. Should β not be larger than zero, the climber would not move upward. Moreover, since the motor's torque production decreases monotonically with climber velocity, a climber with $\beta \leq 0$ would always operate above the null-cline in state space; in essence, it would be unable to climb.

Finally, $\sigma > 1$ is established as a convenient sufficient condition to simplify the proof and is handily achieved by our platforms (Table 5). Specifically, $\sigma > 1$ assures that both eigenvalues of the system are real and negative (see appendix for exact expression), with $\lambda_1 > \lambda_2$. From the definition of σ, it is evident that $\sigma > 1$ for any climber reasonably similar to DynoClimber. Only an extremely under-geared climber could cause σ to fall below 1; DynoClimber would have to employ a gear ratio of roughly 14:1 instead of the nearly 57:1 gearing used in the most recent version of the robot.

Proposition 2. *Defining $I = [0, \zeta_B]$, the return map R has a bounded slope over this interval: $\forall\zeta \in I$, $DR(\zeta) \in (0, 1)$.*

Proof. First we show that R is strictly monotonic: $DR(\zeta) > 0$. To that end, we examine DR from (13),

$$DR(\zeta) = \frac{(2\rho)(e^{-\alpha\sigma T})(d)}{\rho(d^2+1) + c(d^2-1)},$$

and demonstrate that its numerator and denominator have the same sign (in this case, positive).

We note that $\rho > 0$, since $\zeta > 0$ (the climber begins with a positive velocity), $\alpha > 0$ (there is an energy storage spring) and $\sigma > 0$ (stall torque and no-load speed are positive).

Since $d > 1$ by inspection, each term in this expression is positive if $c(\zeta) = \beta - \alpha\sigma\zeta > 0$. Noting that $c(\zeta)$ is strictly decreasing in ζ, it is evidently minimized over $\zeta \in I$ when $\zeta = \zeta_B$. Expanding $M \cdot c(\zeta)$ into physical parameter values and simplifying,

$$\begin{aligned} M \cdot c(\zeta) &= (-Mg + kl_s + F_s) - \frac{F_s}{2}\cdot\frac{\zeta}{v_{nl}} \\ &= -Mg + kl_s + F_m(\zeta) + \frac{F_s}{2}\cdot\frac{\zeta}{v_{nl}}, \end{aligned}$$

where F_m is the vertical force produced by the motor as a function of velocity. To evaluate c at $\zeta = \zeta_B$, we recall the meaning of ζ_B: this is the velocity at which the climber has a net acceleration of zero at the beginning of a stride. Thus, $F_m(\zeta_B) = Mg - kl_s$, implying that

$$c(\zeta_B) = \frac{F_s}{2}\cdot\frac{\zeta_B}{M\cdot v_{nl}} > 0.$$

Since $c(\zeta) > 0$ over I, $\forall\zeta \in I$, $DR(\zeta) > 0$.

Next, we demonstrate that $DR < 1$.

We aim to show that the numerator of $DR(\zeta)$ is smaller than its denominator. Subtracting the numerator of (13) from the denominator and simplifying:

$$\begin{aligned} &\rho(d^2+1) + c(d^2-1) - (2\rho)(e^{-\alpha\sigma T})(d) \\ &\quad > \rho(d^2+1) + c(d^2-1) - 2\rho d \\ &\quad = \rho(d-1)^2 + c(d^2-1) > 0. \end{aligned} \quad (38)$$

Table 5. Parameter assumptions applied to models from Table 3.

Quantity	Assumption	Initial model	Revised model
β	> 0	161	197
σ	> 1	27.5	16.6
α	> 0	4.92	4.72

Thus, $DR(\zeta) < 1$ for all $\zeta \in I$. □

Proposition 3. *For all $\zeta \in I$, $R(\zeta) \in I$.*

Proof. Since Proposition 2 establishes that R is monotonically increasing with slope less than 1 over I, we need only demonstrate that $R(0) \geq 0$ and that $R(\zeta_B) \leq \zeta_B$ to establish the invariance of I. Using the return map derived in (12) and noting that $\lambda_1 \cdot \lambda_2 = 1$,

$$R(0) = \frac{\beta}{2\alpha\sqrt{\sigma^2 - 1}} \cdot (e^{\alpha\lambda_1 T} - e^{\alpha\lambda_2 T}).$$

Since $\lambda_1 > \lambda_2$ and all other constants are positive, $R(0) > 0$ for any $T > 0$.

Looking at the flow of the system beginning at $\zeta_B =: \ell_2(\mathcal{N} \cap \mathcal{L}_1) = \frac{v_{nl}(F_s + kl_s - gM)}{Fs}$, we show that the system's trajectory remains above $\mathcal{N}$ on the (z_1, z_2) plane by looking at the vertical distance between the two:

$$\ell_2 \circ f^t \circ \ell_2^{\dagger}(\zeta_B) - \left(\frac{\beta}{2\sigma\alpha} - \ell_1 \circ f^t \circ \ell_2^{\dagger}(\zeta_B) \cdot \frac{\alpha}{2\sigma}\right) \quad (39)$$

$$= \frac{\left(e^{t\alpha\lambda_1} - e^{t\alpha\lambda_2}\right)\beta}{8\alpha\sigma^2\sqrt{\sigma^2 - 1}} \geq 0. \quad (40)$$

Again, since $\lambda_1 > \lambda_2$, the expression above is positive. This demonstrates that the climber's velocity stays above the null-cline $\mathcal{N}$ throughout the stride, implying that the climber's velocity is strictly decreasing. Thus, $R(\zeta_B) < \zeta_B$. □

Corollary 2. *The inertia I is attractive from above.*

Proof. For all $\zeta > \zeta_B$, $f^t \circ \ell_2^{\dagger}(\zeta)$ lies above $\mathcal{N}$ on the (z_1, z_2) plane. Thus, for any initial condition $\zeta > \zeta_B$, $R^n(\zeta) < \zeta_B$ for sufficiently large n. □

Proposition 4. *For all $\zeta_0 \geq 0$, iterates of the return map $R^n(\zeta_0)$ converge to a fixed point, ζ^*, as $n \to \infty$.*

Proof. We proceed by demonstrating that R is a strict contraction in I and applying the contraction mapping principle. Thus, we first demonstrate that $\forall \zeta_1, \zeta_2 \geq 0$, and $\zeta_1 \neq \zeta_2$, $|R(\zeta_2) - R(\zeta_1)| \leq k \cdot |\zeta_2 - \zeta_1|$, where $k \in (0, 1)$.

Here $|R(\zeta_2) - R(\zeta_1)| = |\int_{\zeta_1}^{\zeta_2} DR(\zeta)\, d\zeta|$. Since $DR < 1$ by Proposition 2, and DR is continuous on I, DR must never exceed some $k < 1$ on the interval I. Thus, $|\int_{\zeta_1}^{\zeta_2} DR(\zeta)\, d\zeta| \leq |\int_{\zeta_1}^{\zeta_2} k d\zeta| = k|\zeta_2 - \zeta_1|$.

Since R is a strict contraction on a complete space I, it has a unique fixed point with I as its basin of attraction by the contraction mapping principle. Moreover, since I is attractive from above, the fixed point of R has a basin of attraction of $\overline{\mathbb{R}^+}$. □

Appendix C: Index to multimedia extensions

The multimedia extension page is found at http://www.ijrr.org

Table of Multimedia Extensions

Extension	Type	Description
1	Video	Initial version of DynoClimber (30 cm/s)
2	Video	Modified version of DynoClimber (67 cm/s)